Utrecht University

Graduate School of Natural Sciences

Modelling ultrafine particles concentrations near highways

Master Thesis

Rens van Eck

Supervisors:

Prof. Dr. Ir. G.J.M. Velders

Dr. R. Holzinger

Institute for Marine and Atmospheric research Utrecht

July 18, 2024

Acknowledgements

I would like to extend my deepest gratitude to several individuals who have helped me undertake this thesis.

First and foremost, I am profoundly grateful to my supervisor Prof. Dr. Ir. Guus Velders for his invaluable guidance and academic insights in the course of this project. Our weekly meetings and discussions were crucial in charting a productive course, and to overcome the many hurdles on our path. Furthermore, I would like to thank Dr. Joost Wesseling, Dr. Sjoerd van Ratingen and Dr. Anneke Batenburg from the National Institute for Public Health and the Environment (RIVM) for their expert advice and providing the measurement data used in this thesis. Their contributions have steered the development of the model towards a useful state. Lastly, I would be remiss in not mentioning my family, especially my partner Jurgen and brother Mark. Their support, and willingness to be my sounding board, has kept my motivation high during an intense academic year.

Abstract

Ultrafine particles (UFPs) are particles in the ambient air with a diameter less than 100 nm. Their potential impact on human health is a growing field of research. This thesis investigates the physical and chemical behaviour of UFPs near a highway, and how the distribution changes with increasing distance from the highway. We focus on modelling their evolution using an implementation based on the HAM/SALSA2.0 model, and compare the results to preliminary measurements. This implementation simulates a constant source of particles and their dispersion through the system. Measurements showed that particles smaller than 20 nm were the most numerous class near the highway, but their numbers quickly diminished with increasing distance, until the distribution became indistinguishable from the local background distribution after only a few hundred meters. A number of sample emissions characteristic of diesel and gasoline vehicles were simulated, and their results were observed to have similar characteristics as to what is seen in observational data. The modified model's sensitivity to temperature, humidity, air pressure, and the newly-implemented dispersion mechanism was investigated. We found that the relation between the simulated UFP concentrations and the meteorological variables is qualitatively similar to those seen in measurements. A non-linear relation between simulated UFP concentrations and dispersion rate was found, likely due to competing mechanisms.

The image on the title page shows smog over a busy highway, which is in part caused by the emission of particulate matter and ultrafine particles. (Credits: Intermountain Medical Center, found at EukerAlert.org)

Lay summary

Air quality plays a large role in human health and lifespan. Millions of people die every year from diseases caused by air pollution, such as heart and lung diseases, and cancer. One of the components of air pollution which has come into the focus of attention recently, is ultrafine particles (UFPs). These are particles smaller than 100 nanometers. These are believed to be especially dangerous, because they may be able to enter our bodies directly, by passing through the lungs into the bloodstream, and cause serious health problems.

One aspect of UFPs that is not yet well understood is how they move and behave. Therefore, the main topic of this thesis is understanding how these UFPs behave near highways, because highway traffic is a significant source of UFPs. These particles are then transported away by the wind. Our aim was to see how far these particles travel, and how their concentrations change over relatively short distances and times. We used a combination of measurements and a computer model called HAM/SALSA2.0 to study this. This model can simulate how particles behave in the air. We modified the model to include a constant source of particles, and to spread the particles through the system. By doing this, we hoped to simulate the observations made in the measurement data.

It was found that the concentration of the smallest UFPs decreases quickly as you get farther away from the highway. It takes only a few hundred meters for their concentrations to drop to background levels. We were able to reproduce these findings with the model, where a stable background also quickly appeared. We also studied how weather conditions such as temperature and humidity affect the concentrations of these particles. We found that the patterns seen in the model matched those seen in measurements.

However, this model also has some limitations. It is difficult to directly relate the model's results to real-world conditions such as wind speed, or at what distance a stable background of particles appears. The model also assumes that the UFPs consist of six types of substances, in certain proportions. This consistency may vary depending on the source of the UFPs. Furthermore, the model cannot simulate the production of new particles from gaseous vehicle emissions, which is a large portion of air pollution.

To improve the model, future research could adjust how particles move in and out of the modelled system. Finding a way to relate the model's results to real-world conditions is important for understanding the model's applicability. Besides this, more measurements at varying distances from highways are needed, to see if the patterns seen in this study occurs in more environments.

Contents

1 Introduction

Air quality has a significant effect on human health and life expectancy [WHO, 2016]. Globally, millions of people die each year from diseases caused by air pollution, including pulmonary and cardiovascular diseases, as well as various cancers [Nadadur and Hollingsworth, 2015]. Moreover, air pollution has been found to be one of the leading causes of premature deaths due to cancer [Vineis and Husgafvel-Pursiainen, 2005]. A key component of air pollution is particulate matter [Mukherjee and Agrawal, 2017], and particularly the subclass of ultrafine particles (particles smaller than 100 nm) has garnered the attention of researchers in recent years for its harmful effects on health [Schraufnagel, 2020], [Gezondheidsraad, 2021]. To better understand the health effects and exposure of ultrafine particles, we also need to understand their spatial and temporal profiles. Ultrafine particles are highly dynamic and their concentrations can vary significantly over short distances and timescales. This is particularly the case in the urban environment and near highways, with the smallest particles disappearing relatively quickly and the measured distribution becoming indistinguishable from the background [Zhu et al., 2002]. The large amounts of traffic on highways serve as a strong source of ultrafine particles, which are then transported away from the highway by wind.

The main objective of this thesis is to understand the particle dynamics on the scale of several hundred meters away from a highway. We aim to implement a model that can reproduce the lack of observation of the smallest particles at a relatively short distance and time from a highway, after which a stable background remains. This is achieved by modifying an existing aerosol box model, HAM/SALSA2.0, to which we add the ability to simulate a constant influx of particle emissions and the dispersion of particles in the system. This may eventually be used to determine effective emissions, based on which the transport and evolution of UFP on larger scales may be simulated without explicitly simulating particle microphysics. Therefore, the goals of this study are to determine how quickly a stable particle distribution appears in the model after initialisation, and how the particle concentrations depend on temperature, humidity, air pressure, and the dispersion rate parameter of the model.

Section 2 begins by giving a comprehensive review of the various dynamic processes affecting the formation and interaction of ultrafine particles, as well as their sources. A detailed discussion of the model implementation is given in Section 3. A number of emissions profiles representative of diesel and gasoline engines are simulated. The model findings are compared to a preliminary measurement series, which measured particle distribution on varying distances from a highway. Additionally, we investigate the model's dependency on the environmental variables of temperature, humidity, and air pressure. The effect of dispersion on particle concentrations in our implementation is studied in additional detail, with particular attention to identifying a non-linear relation. The results, and their discussion, of these investigations are shown in Section 4. Finally, Section 5 concludes the thesis by summarising our findings, relating them to previous research and giving recommendations for future research.

2 Theoretical background

The key components of air pollution that draw significant attention are ammonia (NH_3), sulfur dioxide (SO_2), nitrogen dioxide (NO_2), ozone (O_3), and particulate matter (PM). These may combine in extreme pollution events to create smog, which can cause immediate health effects such as shortness of breath and irritation of mucous membranes [RIVM]. Particulate matter, or aerosols, are agglomerates of solid or liquid particles suspended in the air and may be found in a wide range of sizes. The most common way of characterising their size, is by aerodynamic diameter D_p. Using this parameter, a number of classes of particulate matter have been defined. These are PM_{10}, $PM_{2.5}$ and PM_1, where PM_d includes all particles with $D_p < d$ µm. Additionally, in more recent years, another class has been added to this list; $PM_{0.1}$, alternatively called ultrafine particles (UFPs) [Abdillah and Wang, 2023]. These are particles with an aerodynamic diameter less than 0.1 µm (100 nm). Alternatively, PM may be categorised in various "modes", the bounds of which are not very strict. Shown in the bottom portion of Figure 1, there are the nucleation mode (< 10 nm), the Aitken mode (10 - 100 nm, included in the nucleation mode in the figure), the accumulation mode (100 nm - 1 µm), and the coarse mode (> 1 µm).

The most commonly used ways to describe PM are by number concentration and mass concentration. The two largest classes of particulate matter, PM_{10} and $PM_{2.5}$, sometimes also called coarse and fine particulate matter respectively, are usually described in terms of mass distribution. This reflects one manner of how concentrations of these particles are measured; ambient air is passed through filters for a certain time. The difference in weight of the filter before and after determines the concentration of particulate matter in the air [Quincey and Butterfield, 2009].

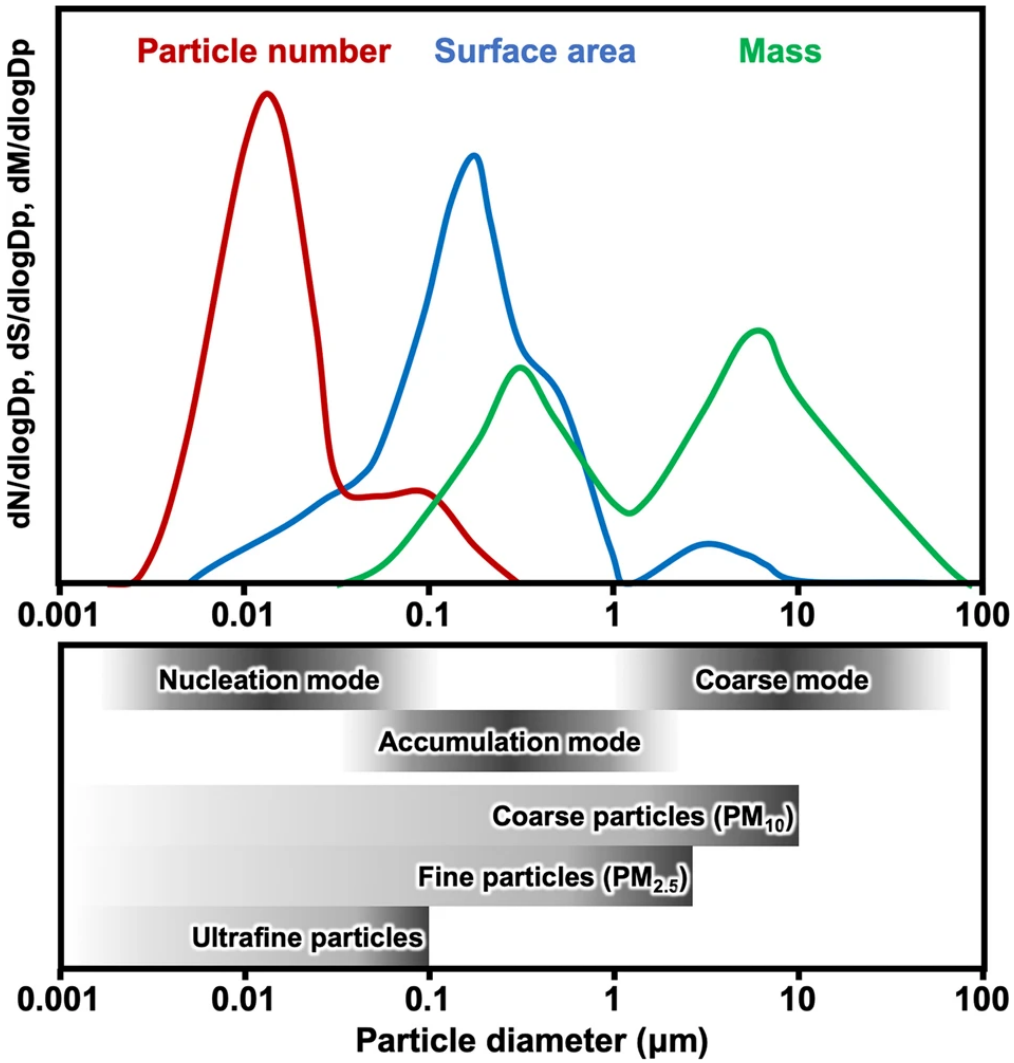

Figure 1: The top portion shows a schematic of a typical ambient particle distribution. Red shows number concentration ($d\mathrm{N}/d\mathrm{logD}_p$), blue shows surface area concentration ($d\mathrm{S}/d\mathrm{logD}_p$) and green shows mass concentration ($d\mathrm{M}/d\mathrm{logD}_p$). The bottom portion shows three commonly used modes of describing atmospheric aerosols; the nucleation mode, the accumulation mode and the coarse mode. Figure from [Kwon et al., 2020]

Compared with PM_{10} and $\mathrm{PM}_{2.5}$, UFPs or $\mathrm{PM}_{0.1}$ are best characterised by their number concentration. This is due to UFPs having negligible mass, but constituting the majority, accounting for $80-90\%$, of particle numbers in ambient air [Hofman et al., 2016]. As such, given the focus of this study, all results pertaining to particle concentrations will be presented in terms of number concentration.

A notion of "characteristic particle count" is employed often in this investigation. Seeing as we've used a 0D box model to simulate various scenarios (see Section 3.1), there is no clear notion of size. Instead, we rely on the rough order of magnitude of the amount of particles in the system. The number of particles, particularly in UFPs, has consequences on the effectiveness of various dynamic processes. When particle counts are relatively low, particles do not encounter one another as often as when particle counts are relatively high. This

means that e.g. coagulation would not work as strongly for low counts as for high counts. In the context of our work, this necessitates careful consideration of particle counts that are characteristic of the specific scenarios under study, as there can be a marked difference between roadside and background measurements [Chatain et al., 2021].

2.1 Sources of ultrafine particles

Ultrafine particles are a subset of particulate matter with a diameter of less than 100nm [Li et al., 2016]. Drawing on the literature study by [Moreno-Ríos et al., 2022] for a general overview, it is known UFPs are formed by dynamic processes such as nucleation, condensation, coagulation, and dispersion. They mainly consist of organic compounds, elemental/black carbon, sulphates, nitrates, and trace metals. A study by [Cass et al., 2000] using measurements made in seven cities in Southern California, shows that UFPs on average consist of 50% organic matter, 14% trace metal oxides, 8.7% elemental carbon, 8.2% sulphate, 6.8% nitrate, 3.7% ammonium ions, and small amounts of trace elements. Reporting only on organic matter and various salts of sulphate and ammonium, [Kuhn et al., 2005] found similar average particle compositions for measurements made 5 km downwind of a park in Pittsburgh, Pennsylvania. Sources of UFPs can be both biogenic and anthropogenic, and are quite varied. Forest fires and sea salt sprayed from the ocean are known sources of UFPs, as well as spontaneous combustion of coal waste in mining site [Dias et al., 2014] and aircraft [Janssen et al., 2022]. Particularly in background locations where other forms of pollution are relatively rare, the role of biogenic volatile organic compounds (BVOCs) in new particle formation has been found to be significant [Kammer et al., 2020]. Some plants produce compounds like isoprene and terpenes, which can react to form new particles [Ehn et al., 2014]. With SO_2 emissions being projected to decrease further in the Netherlands [Smeets, 2023], the role of this mode of new particle formation is thought to become more important [Dada et al., 2023]. In this study, we are mainly interested in the anthropogenic sources of UFPs such as combustion of fossil fuels or biomass, vehicular traffic and industrial emissions, which are still the largest source of UFPs [Moreno-Ríos et al., 2022].

Many studies have shown that the emissions of motor vehicles constitute a major portion of the ultrafine particles found in the urban environment [Fruin et al., 2008], [Bigazzi and Figliozzi, 2012], [Choi et al., 2013]. There is a slight difference in emissions between diesel and petrol engines, namely that heavy duty diesel vehicles have been measured to produce up to 24 times more particulate matter per unit mass of fuel burned than light duty vehicles [Morawska et al., 2008]. The distribution of sizes are also slightly different, as diesel engines produce particles mostly within the 60 to 120nm range, close to lognormally distributed, whereas petrol engine emissions are more asymmetric, with mean diameters in the range of 40 to 80nm [Harris and Maricq, 2001]. Moreover, particle emissions can be broadly categorised into classes, depending on where the particles are produced. Primary particles are produced in the engine or exhaust system, whereas secondary particles are produced after emission from the exhaust system [Charron and Harrison, 2003], [Ntziachristos et al., 2007]. Primary particles are mostly carbonaceous agglomerates of particles ranging anywhere between 30 and 500nm in diameter, most of which residing in the accumulation mode. Secondary particles are formed when the hot exhaust gases cool rapidly and condense to form small particles through nucleation (more info in Section 2.2). These mainly consist of hydrocarbons and

sulphuric acid, and most are up to 30nm in diameter [Morawska et al., 2008].

2.2 Dynamic Processes

A lot of information of the dynamical processes of the formation of UFPs can be found in [Pandis and Seinfeld, 2016] and the study by [Moreno-Ríos et al., 2022]. The following text is largely based on these works. Gas particles do not instantly transform to liquid or solid phase the moment it becomes energetically favourable to do so. Instead, small nuclei need to form first, for gas particle to condense onto. This is similar to how water condenses into droplets. Once the concentration of gas particles has grown to a sufficient level, they may spontaneously form small nuclei in a process called *nucleation*. The nucleation of gases can occur on nuclei comprised only of the present gas molecules, called homogeneous nucleation, or on foreign substances, called heterogeneous nucleation [Pandis and Seinfeld, 2016, Chapter 11]. A significant fraction of the total number of particles present in the atmosphere is formed originally by nucleation from the gas phase, a process known to occur virtually throughout the troposphere. It is thought that sulphuric acid (H_2SO_4), formed by combining water with emitted SO_2, is the essential precursor gas for most nucleation events [Curtius, 2006].

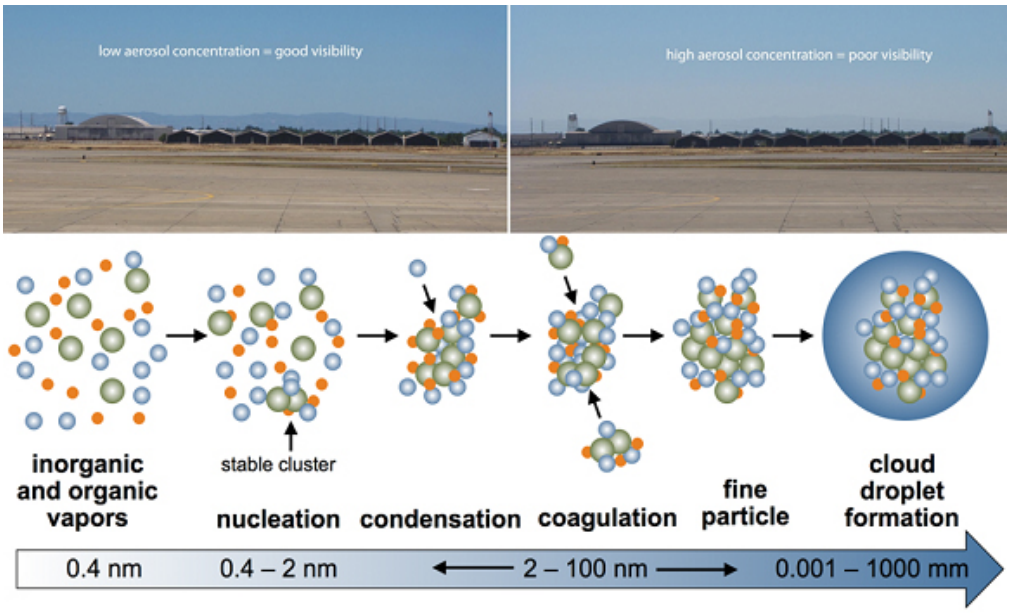

Figure 2: Schematic of the dynamic processes involved in new particle formation (NPF). The top part shows the visible effect of higher aerosol concentrations. Figure from [PNNL, 2016]

Figure 2 gives a schematic overview of the dynamic processes involved in new particle formation (NPF), starting at the vapour/gas phase, ending at cloud droplet formation. This last step is not particularly interesting for our investigation, but does serve as an intuitive anchor, as illustrated by the top part of the image. The more polluted the air is, the more aerosols can form, some of which may grow large enough to participate in cloud droplet formation, further limiting visibility and producing the haze often associated with air pollution.

After a nucleus has formed, additional molecules from the gas phase may start accumulating, in a process called *condensation*. This causes the nucleus to grow into a larger aerosol particle, increasing the number of larger particles and decreasing the number of smaller particles. More concisely, a particle population that is growing due to condensation alone, has a size distribution that is moving to the right [Pandis and Seinfeld, 2016, Chapter 13].

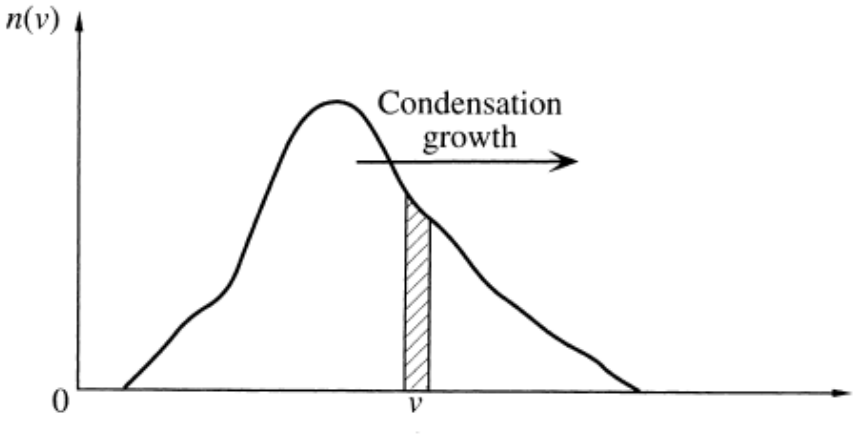

Figure 3: Schematic of the movement of a particle distribution under the effects of condensation. Here v denotes particle volume $v = \frac{1}{6}\pi D_p^3$ where D_p is particle diameter, and $n(v)$ is the number of particles as a function of volume. Adapted from [Pandis and Seinfeld, 2016]

Aerosol particles may come into contact with one another, e.g. as a result of their Brownian motion, and stick together to form larger aggregates. This process is called *coagulation*. This mechanism potentially reduces the amount of small particles, while increasing the number of larger particles in return. There are varying conclusions in literature regarding the importance of coagulation depending on ambient conditions. There are studies that associate a large amount of larger particles with coagulation in the conditions found near a highway [Zhu et al., 2002], [Rim et al., 2012]. This process was found to act on such timescales, that measured concentrations could not be discerned from the background concentrations. On the contrary, other studies have found that the effects of coagulation are negligible in urban ambient conditions [Pohjola et al., 2006].

Another key process that influences the local concentration of UFPs and particulate matter in general, is *dispersion*. Given the importance of this process for the remainder of this study, extra attention is brought to this subject in Box 1.

Besides formation processes, there are also removal processes at play. It is common to make a distinction between dry and wet removal processes, though the physical processes involved in both types are fundamentally the same [Prodi and Tampieri, 1982]. In the former, commonly called *wet deposition*, aerosols (or particles in general) are removed from the air either by e.g. rainfall, or by functioning as cloud condensation nuclei (see Figure 2.

Aerosol particles are incorporated into rain or cloud droplets, which then fall to the ground [Yamamoto, 2023]. In the latter, usually referred to as *dry deposition*, aerosol particles are removed from the air by colliding with a surface and sticking to it [Kurppa et al., 2019]. This can occur by particles colliding with objects on the surface due to wind. Alternatively, particles may stick to the ground due to a process called gravitational sedimentation, in which they essentially sink due to their mass. Relatively large aerosols are particularly affected by this, which would allow UFPs to remain in the air for longer periods of time than larger particles [Abdel-Shafy and Mansour, 2016].

3 Methods and data

Explain SALSA2.0 configuration as box model, parts added to the SALSA2.0 framework (wind and diffusion), and justify the selection of the settings, both environmental and physical. Introduce measurement data, explain the pre-processing steps done on the data such as selection based on direction of wind, show map of the measurement station, images of filtered data.

3.1 Model

We used the SALSA2.0 sectional aerosol module [Kokkola et al., 2018] within the Hamburg Aerosol Model (HAM) version 2.3 framework, run as a 0-dimensional (0D) box model. Note that we did not make use of the more common version of the model HAMMOZ, which contains the MOZ chemistry model as well. This means that sulfate chemistry is also modelled by the schemes present in HAM.

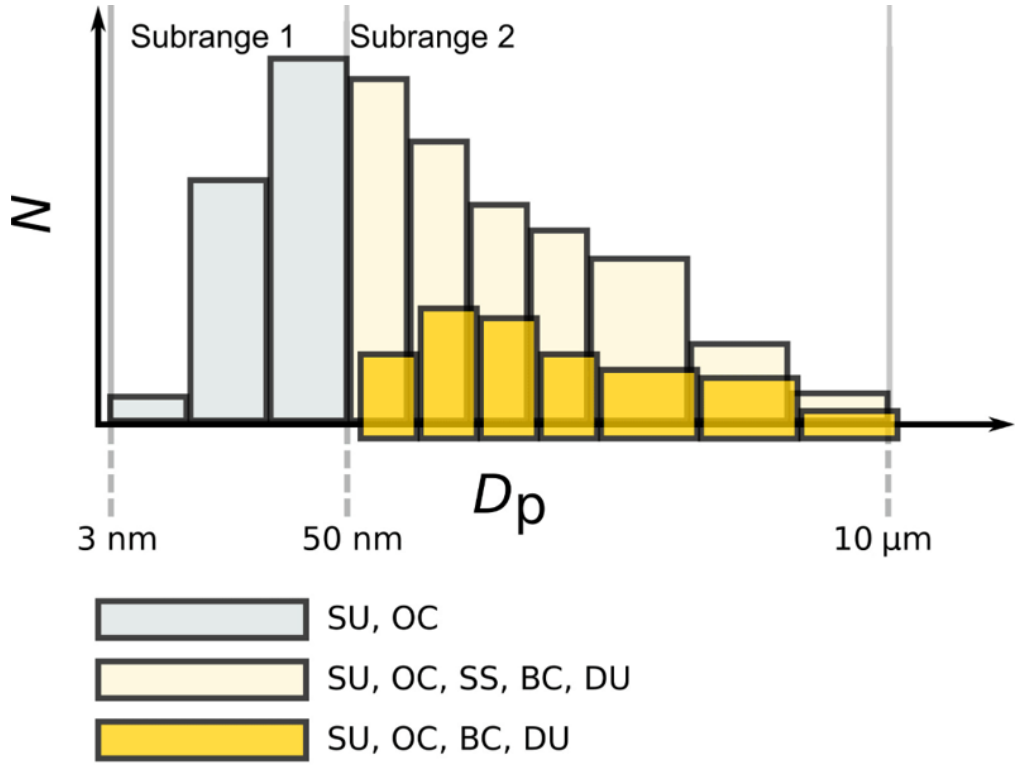

Figure 4: Schematic of the number size distribution as a function of aerosol diameter used in SALSA2.0. D_p is the aerodynamic diameter of an aerosol particle. The bottom shows which "compounds" are used in SALSA2.0: sulfate (SU), organic carbon (OC), sea salt (SS), black carbon (BC), and mineral dust (DU). Adapted from [Kokkola et al., 2018]

Sectional aerosol models work by dividing particle distributions up into bins, or sections, based on the aerodynamic diameter D_p of the particles. Furthermore, as shown in Figure 4, the model employs two subranges: subrange 1, spanning particle diameters $D_p = 3 - 50nm$ and subrange 2, spanning particle diameters $D_p = 50nm - 10\mu m$. The two subranges shown

at the "back" of the figure, in light-grey and off-white, are treated as being soluble, whereas the part of subrange 2 at the "front" in yellow is treated as being insoluble. The chemical compounds listed at the bottom of the figure, can be seen compound classes used by HAM, and each represents a number of chemicals. These are sulfate (SU), organic carbon (OC), sea salt (SS), black carbon (BC), and mineral dust (DU). The two subranges at the back of the image are henceforth going to be referred to as population A (soluble particles), and the front part of subrange 2 will henceforth be called population B (insoluble particles). To further clarify the naming convention by means of example, the third bin of the first subrange is then called "2a3". The fourth bin in population B, would similarly be "2b4". Given that the population B only starts at 50 nm and our interest also includes particles smaller than that, we will be presenting model results of population A, soluble particles.

A schematic flowchart of the operation of our implementation is shown in Figure 5 below. All processes discussed in Section 2.2 are implemented in SALSA2.0.

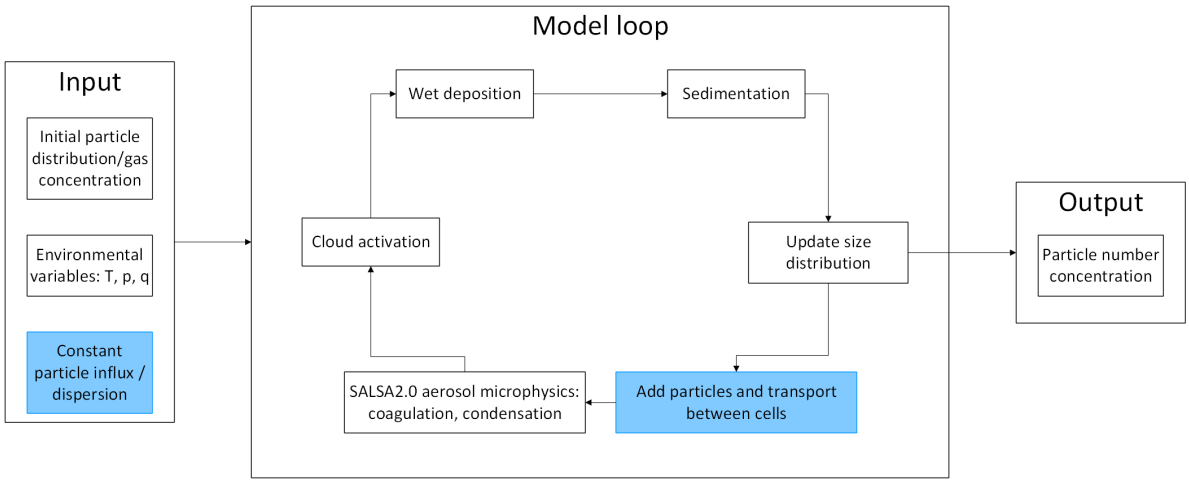

Figure 5: Schematic flowchart of our model's operation. The blue colour highlights the constant particle influx and dispersion between cells, mirroring the blue arrows seen in Figure 6.

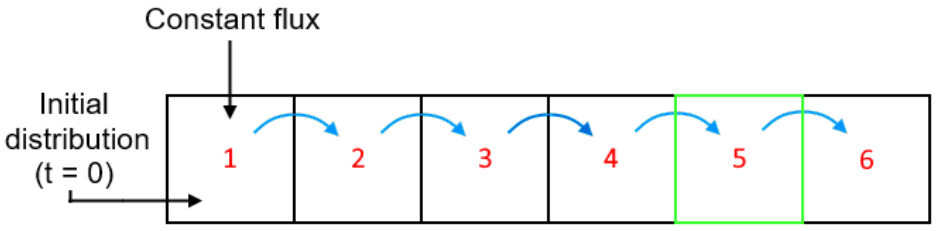

Figure 6: Schematic of the model setup. The blue arrows indicate the transport/dispersion between cells. The output of cell 5 (green) is monitored, to allow for the effects of distance (through dispersion) to take place.

Conceptually, our implementation of the model simulates how long it takes for a constant background concentration to establish itself. The model was set up as a 1D line of six 0D

grid cells, as shown in Figure 6. These cells are initially independent from one another. Because the individual cells are 0D, there is no real notion of size. Size, instead, is implied by the characteristic number of particles in the cell - a lower concentration of particles would imply a larger cell, as a larger cell distributes particles over a larger volume. To simulate the effect of spatial transport and the accompanying effect of dispersion, each cell transports only a portion of its contents to the next cell over. The rate at which this transport occurs, is similarly dependent on the implied size of the cells; smaller cells would be expected to transport their particle faster from one to the other, given equal wind speeds. More information about the mechanism of dispersion in this implementation is given in Box 1.

Box 1 | Dispersion

Dispersion involves the spread of particles away from their source through e.g. wind and turbulence. The further one moves away from a source of UFPs, the lower the number concentration of particles one expects to be, due to the particles dispersing into a larger volume of air. As such, factors like wind speed, atmospheric stability and topography play a crucial role in the dispersion of particulate matter. Particularly in urban environments, it is found that periods with low wind speeds and high vertical stability are associated with the highest particulate matter counts, and thus the largest effect on human health [Muñoz and Corral, 2017].

In the context of our implementation of the model, dispersion refers particularly to the (partial) transport of particles from one place to another. In Gaussian plume modeling, the concentration of a pollutant downwind from the source disperses from the plume's center line according to a normal distribution, expanding both horizontally and vertically. Besides the three factors named above, ambient temperature and the altitude of the pollutant source are known to affect dispersion as well [Abdel-Rahman, 2008]. Given that our implementation works in a 0-dimensional box model, there is no clear notion of size or distance. Instead, our model transports $d\%$ of the aerosol contents in every size bin from grid cell i to grid cell $i+1$ on every time step, where d is called the *dispersion rate* of the model. This number can be set independently from other parameters, though some care should be taken. In order to simulate real-world scenarios, realistic dispersion rates should be chosen. Section A.2 gives a derivation for an approximation for what a realistic dispersion rate might be (around 2%).

It is not trivial to relate the dispersion rate used in our model to real-world quantities such as distance or wind speed. To start, there is no notion of wind speed in the SALSA2.0 box model our implementation was based on. Physically, one could say that a constant wind speed of $1\,\mathrm{m\,s^{-1}}$ persisting for 100 seconds would see a parcel of air transported for 100 m downwind, with dispersion working to expand this parcel of air along the way, decreasing its local concentration. Due to the lack of dimensionality, we can make no such claims. Time is the only quantity we can use to relate to the real world. For example, given a certain input distribution and dispersion rate d, it takes x seconds for a stable background concentration to appear. The connection to the real world must be made through measurements at various distances from a source,

by seeing how far away from a source the measurement becomes indistinguishable from the local background. However, for times $> x$ seconds, where the balance persists and the corresponding measurements at greater distances from the source continue, such a relation becomes meaningless; it's only useful to find the distance/time at which the background "starts".

To bridge the gap to real-world scenarios, the dispersion rate could be related to atmospheric stability. When the atmosphere is unstable, turbulence and thus dispersion is enhanced. Conversely, when the atmosphere is stable, turbulence is decreased, and so dispersion will be decreased as well. The phenomena occurring under different stability conditions are well known [Pandis and Seinfeld, 2016]. A splendid summary of these conditions is found in [Huertas et al., 2021], on whose work the following list is based. Neutral conditions occur when there is no heat transfer between the surface and the ground, eliminating effects of buoyancy. As incoming solar radiation warms the surface, the air above the surface (the surface boundary layer, SBL) is warmed up too, giving rise to convective turbulence. In such unstable conditions, there is usually strong vertical motion. Pollution rising up from the ground is quickly dispersed. Finally, when the atmosphere may become stably stratified, which sees virtually all vertical mixing cease. Under these conditions, there is very little vertical dispersion.

Concentration measurements performed at multiple distance of a stable tracer (such as NO_x) emitted by the same source is a more empirical way of determining the dispersion rate. The tracer is question must be stable, to ensure the only effect on local concentration can be that of dispersion; any chemical reactions that alter its concentration would complicate this approach.

Drawing from the information shown in Figure 5, we can say that at $t = 0$, the highway is "turned on", and grid cell one is initialised with a particle distribution measured close to the highway. An example of such a distribution is shown by the red line in Figure 14. A more detailed discussion of how this was obtained is presented in Section 3.2.2. All grid cells are also initialised with a concentration of gas phase sulphate of $5 \cdot 10^{14}$ particles m^{-3}, or $0.08\,\mu\mathrm{g\,m}^{-3}$, which is kept constant throughout the simulation. This serves as a stable background. Every model time step (1 s), particles are added to the first seven bins of cell one. Subsequently, a number of particles based on the specified dispersion rate is transported from cell i to cell $i + 1$. These particles are then removed from cell i, resulting in a balanced source and sink for every grid cell. After this is finished, the various chemistry and aerosol microphysics calculations of the model are solved. The wet and dry deposition (sedimentation) schemes are solved, and the output of the model is converted to a particle number concentration and written to an output file. To allow for the effects of distance to play a role through the mechanism of dispersion, we elected to monitor the output of grid cell five. As stated, it is not simple to ascribe an (effective) distance to each grid cell with respect to grid cell one.

Our model runs can be broadly categorised into two classes: those fed with emissions with distributions shaped after measurements of diesel vehicle emissions, and those of gasoline vehicle emissions. In the case of diesel, the constant flux of particle added to cell one is based on emission data found by [Harris and Maricq, 2001]. They found that particularly diesel

emissions were described very well by a lognormal distribution,

$$n(lnh) = \frac{1}{\sqrt{2\pi} ln\sigma_g} exp\left(-\frac{ln^2 h}{2ln^2\sigma_g}\right) \quad (1)$$

with a geometric standard deviation of $\sigma_g = 1.68 \pm 0.06$. This function is normalised, and so it needs to be scaled up to fit the emissions numbers more precisely. Furthermore, this function is centered on $h = 1$, but can be modified to be centered on the peak of the characteristic emissions of diesel or gasoline vehicles. Figure 7 below shows this normalised distribution centered on the middle of the measured range, 90 nm.

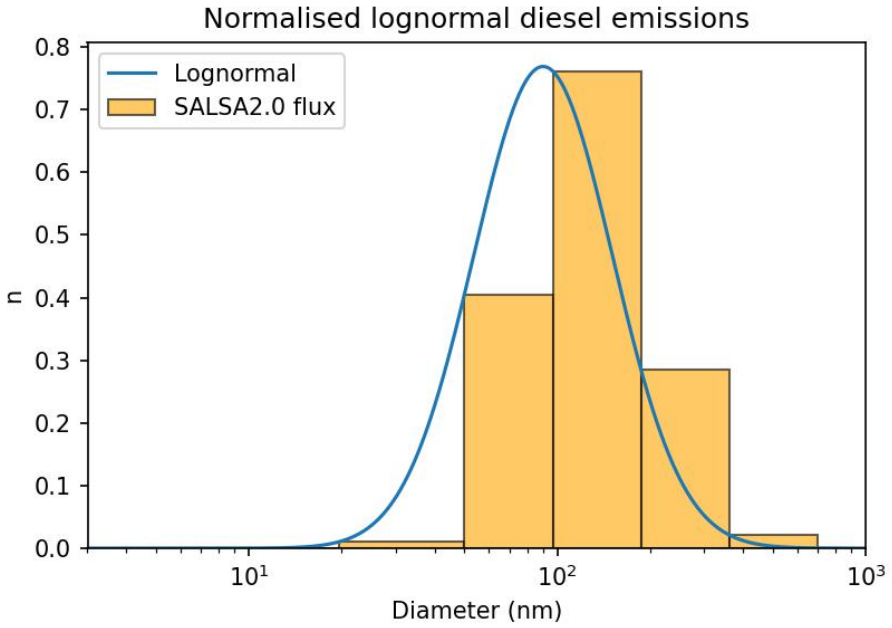

Figure 7: Normalised lognormal curve (blue, based on Equation 1) describing diesel particulate emissions, and corresponding model particle flux translated to bins used in SALSA2.0 (orange).

Primarily the shape of this distribution is what is used when simulating the constant influx of particles as seen in Section 4.1.1. Multiplication by a simple numerical factor can scale the distribution to whichever point is sought, without changing the general shape of the distribution, which is what is typical of engine emissions.

In the case of gasoline vehicle emissions, the distribution of particles is usually found to be more asymmetric [Harris and Maricq, 2001]. Most investigations seem to agree that the particulate matter emitted by gasoline vehicles is predominantly in the nucleation mode, with a portable emission measurement system (PEMS) study conducted in Shanghai, China finding the distribution peaks at 20nm [Huang et al., 2013]. While this study gives valuable insight into gasoline vehicle emissions, their analysis did not report a mathematical function which characterises this distribution. Visual inspection of the distributions they reported seems to suggest that a lognormal distribution as the one described in Equation 1, with $\sigma_g = 1.7$ and a peak located at $D_p = 20$nm is a good approximation for the purposes of the present study. The usage of this distribution is presented with the results in Section 4.1.2.

SALSA2.0 uses many environmental variables, but the ones we focused on most are ambient temperature T, specific humidity q and air pressure p. During our simulations, we kept these values as close to the measured values as possible, to ensure the model performed as close to realistic as possible. The measurement data did not contain values for specific humidity; these were calculated based on measurements of relative humidity and temperature, using an approximation based on the Clausius-Clapeyron relation

$$q \approx RH \cdot \frac{exp\left(\frac{17.67(T-T_0)}{T-29.65}\right)}{0.263p}. \tag{2}$$

In this equation, RH is the relative humidity as a percentage, T and T_0 are the ambient temperature and the reference temperature (273K) in Kelvin respectively, and p is pressure in Pa.

Beyond this, the sensitivity of the model to its environmental variables (temperature, specific humidity and air pressure) was investigated, by feeding the model a certain initial particle number distribution, as well as a constant particle flux, and setting a certain dispersion rate. Then, two of the environmental variables were varied successively while the third was kept constant. This allowed us to graph the response of the model after a certain amount of time to different temperatures, given a certain input. These findings are presented in Section 4.2.1.

Additionally, the sensitivity to the particle influx and dispersion rate was tested. These parameters are expected to significantly influence the resultant particle number distributions. The sensitivity to dispersion rate may be particularly interesting, as tuning this parameter not only transports particles through the system, but also affects how much time the dynamic processes such as condensation and coagulation have to work. Nucleation was turned off for all model runs, based on the pragmatic motivation that this process generates very large numbers of small particles, where none were measured. This choice was furthermore motivated by the supposition that most nucleation events would have taken place by the time the data with which our model is initialised was measured. The findings of these variations are presented in Section 4.2.2.

3.2 Measurement data

Multiple measurement datasets were used as a means of quantifying model performance. Two datasets measured by RIVM were acquired from stationary stations situated along a busy highway and a busy road in the Netherlands [RIVM, 2023b], [RIVM, 2023a]. Another preliminary dataset was acquired by RIVM along the same highway, where measurements were performed subsequently at different distances from the highway [RIVM, 2024]. All particle concentration measurements were performed using the NanoScan SMPS Nanoparticle Sizer 3910 device. Further details are presented in the following subsections.

3.2.1 Stationary measurements

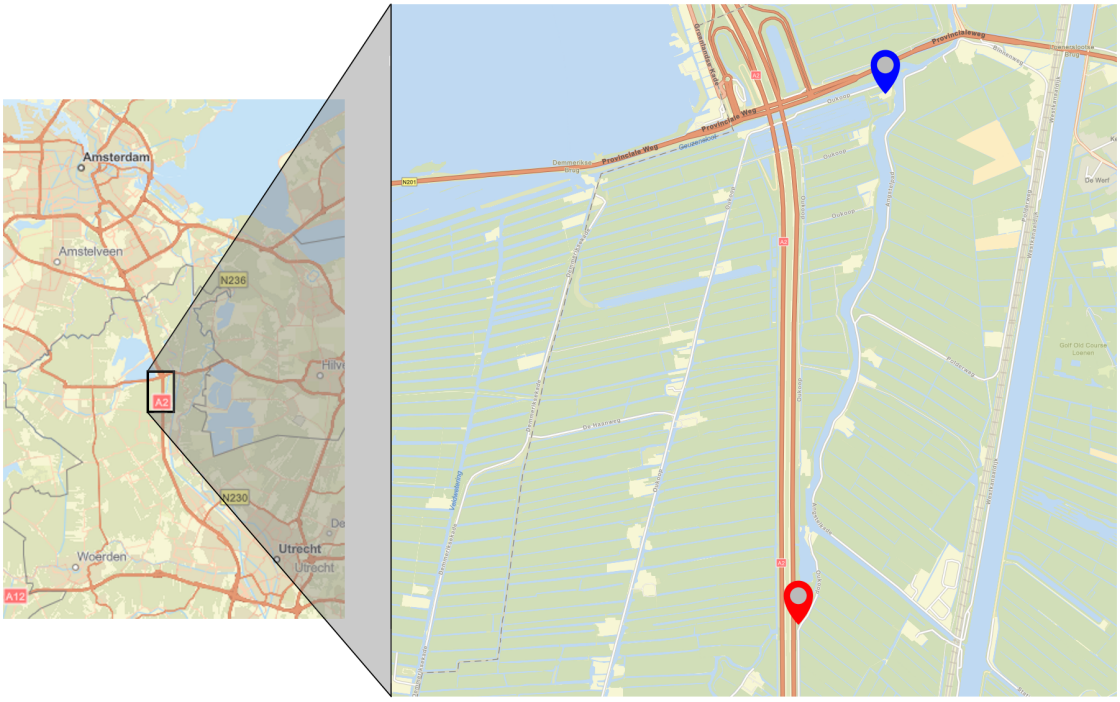

Figure 8: Location of the measurement stations. The red marker denotes location 1, and the blue marker denotes location 2. Adapted from [Google Earth, 2013]

Two datasets, measured by RIVM at two locations, of particle size distributions were used. One dataset was acquired alongside the A2 highway near Breukelen (N52°12′5.4″ E4°59′14.6″) at RIVM measurement station NL10641 (location 1) between July 3$^{\text{rd}}$ and August 16$^{\text{th}}$ 2023. This measurement station is located to the east of a busy highway, roughly 20 m away from the nearest roadway. The other was acquired alongside the N201 (location 2), roughly 2.5 kilometers northeast of the first location, at (N52°13′25.7″ E4°59′37.2″) between May 22$^{\text{nd}}$ and July 3$^{\text{rd}}$ 2023. This station was located some 500 m east of the same highway, but roughly 100 m south of an occasionally busy provincial road. See Figure 8 for a map showing the locations. These stations measure ultrafine particles starting at roughly 7 nm up to 365 nm in 13 channels at a frequency of 1 measurement per minute. At both locations, weather and atmospheric data were measured simultaneously by a Davis weather station, measuring temperature, relative humidity, ambient pressure, wind speed, and wind direction, every 5 minutes along the N201 and every 1 minute at NL10641.

Both SMPS datasets are initially filtered according to the following "rules":

- Drop measurements with reported error status;
- Drop measurements with unrealistic particle counts (total counts $< 1000\,\text{cm}^{-3}$);
- Drop measurements during known maintenance periods (e.g. July 12$^{\text{th}}$ for NL10641)

Subsequently, to make sure we are measuring "fresh" emissions from the roads, particle count data is selected based on the prevailing wind direction during the measurements, uniquely for each location. For location 1, which is close to the roadway lying directly west of it (roughly 70m for the farthest roadway), we selected all data corresponding to winds originating from between 202.5° and 337.5°. For location 2, all data corresponding to winds coming from between 202.5° and 270° were selected as coming from the highway farther away.

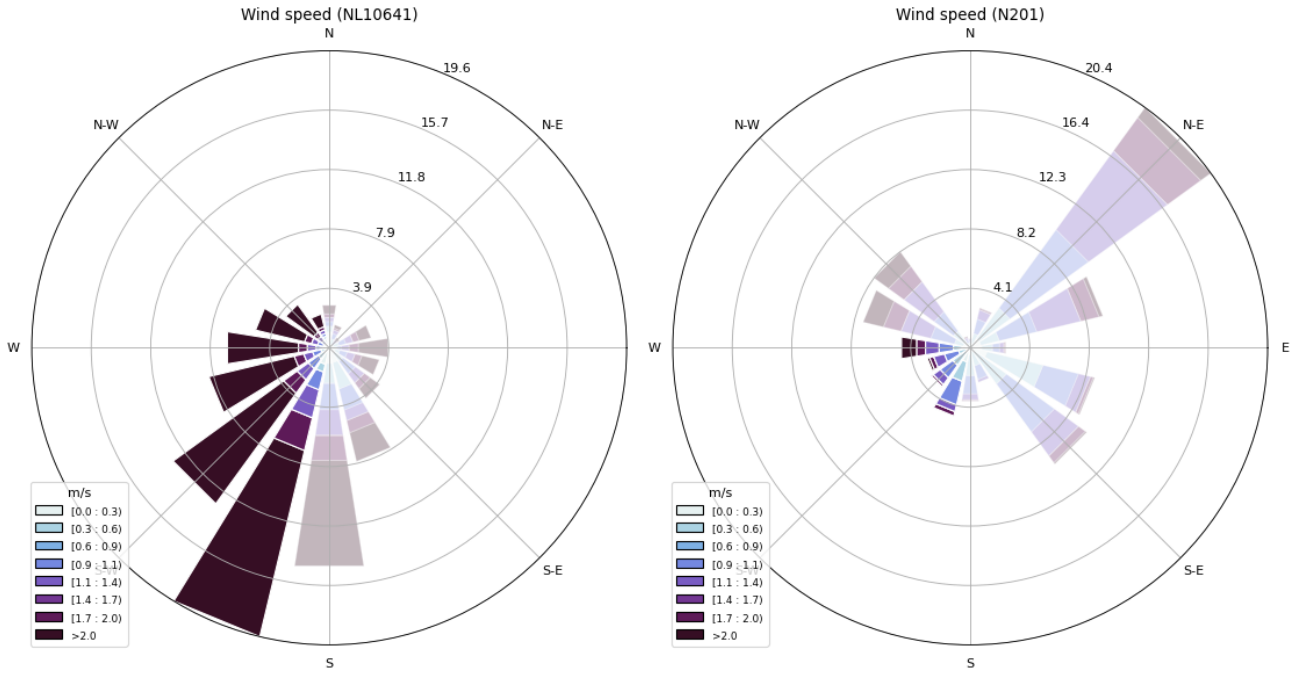

(a) Location 1 **(b)** Location 2

Figure 9: Wind rose of wind speeds at measurement locations. The data in bold colours is selected as coming from the A2 highway. Data from [RIVM, 2023b] and [RIVM, 2023a] respectively.

The data measured while the wind was not coming from the direction of the highway is shown in the fainter colours, is treated as being closer to background concentrations. The corresponding distributions are also given in Figure 10.

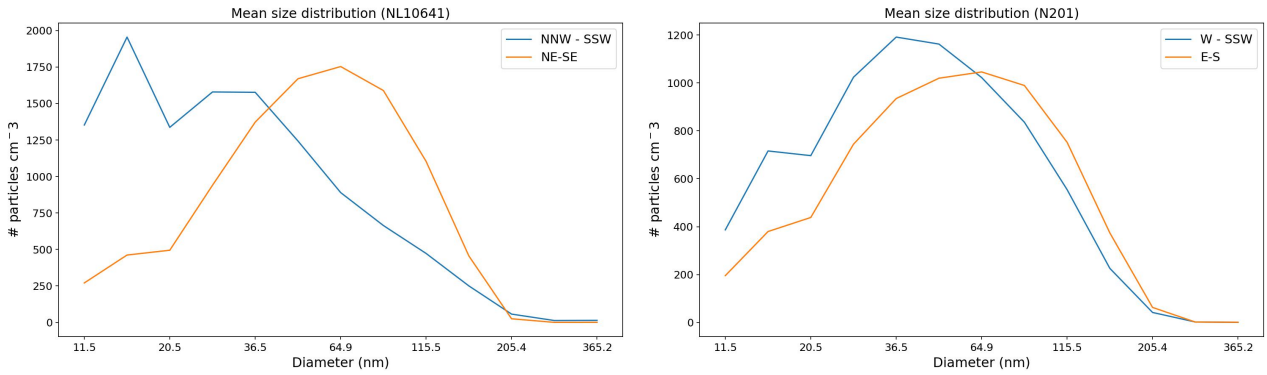

(a) Location 1 **(b)** Location 2

Figure 10: Average measured distributions at measurement locations depending on wind direction. Shown are particle distributions when the wind came from between north-northwest and south-southwest (blue), and between northeast and southeast (orange) for location 1 on the left. On the right between west and south-southwest (blue), and between east and south (orange) for location 2.

Before we were able to compare the measurement data to the modelled data, we had to resample the measurement data to the bins used in SALSA2.0. Based on the assumption that each bin has a linear distribution within it, which is sensible given the hybrid bin method used by SALSA2.0, we calculate the corresponding distribution in SALSA2.0 bins by simple linear interpolation. The result of this process is shown in Figure 11, where we show what the average distribution for the selected wind directions at both locations looks like after resampling (blue lines). It should be noted that this does not explicitly seek to conserve particle counts for every bin.

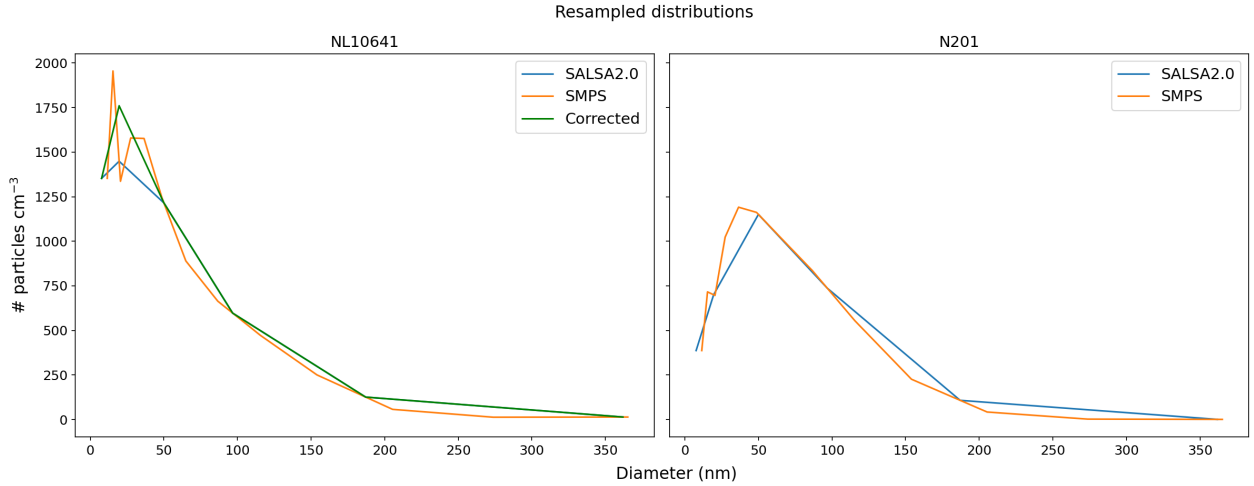

Figure 11: Resampling of the mean distribution measured at location 1 (left) and location 2 (right). The orange lines show the data in its original resolution (bins); the blue lines show what this data looks like after translation to the bins used by SALSA2.0. The green line shows a manually corrected (to better represent the overall shape of the distribution) version of the blue line.

Correlations between the measured aerosol concentrations and meteorological variables were also measured, to see if the model has similar correlations.

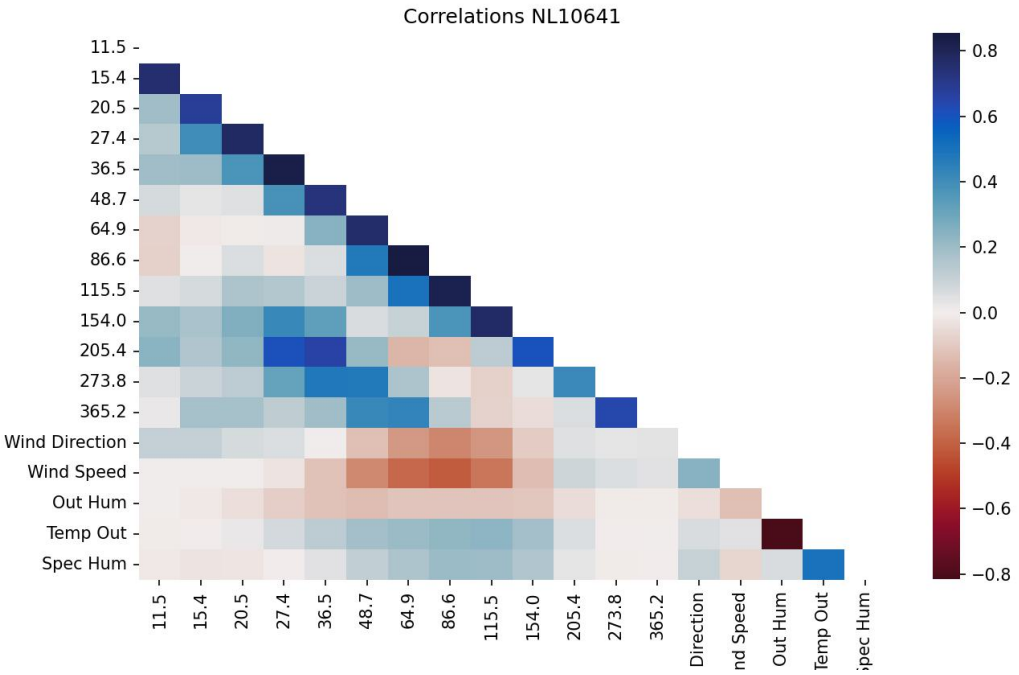

(a) Location 1 (station NL10641)

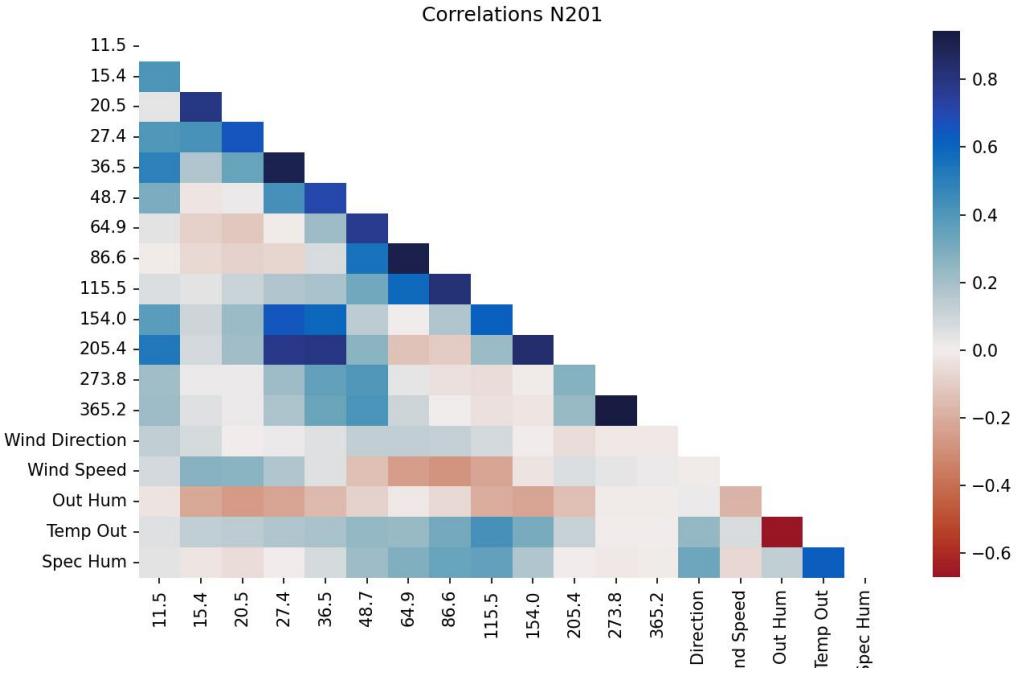

(b) Location 2 (along N201)

Figure 12: Correlation matrices between the measured aerosol concentrations and meteorological variables at measurement location 1 (above) and location 2 (below). The numbers along the axes (e.g. 20.5) are the bin boundaries of the SMPS device in nanometers.

Focusing particularly on the bottom 5 rows, temperature and humidity seem to have a moderately strong effect on particle numbers, particularly in the midrange of 50 to 150 nm for both locations. Wind direction is more strongly correlated with particle numbers for location 1, as it is closer to the highway. As such, wind direction plays a direct role in which emissions are being measured - those close by from the highway, or those further away, i.e. effective background. This is effect is not seen as strongly for location 2, which is further away from the road, and thus already more in a background situation. Both locations show a similar relation for specific humidity, which functions as a compound variable based on humidity and temperature, as shown in Equation 2.

It is notable that there are, generally speaking, no strong correlation between particle numbers of different sizes. This is something that has been found by previous investigations [de Jesus et al., 2019], [Knibbs and de Dear, 2010]. If this were the case, one would be able to devise some way to approximate UFP concentrations based on some proxy measurement.

3.2.2 Distance-dependent measurements

Figure 13: Locations of measurements at varying distances near the A2 highway. Red corresponds to the first location and blue, green and magenta are the second, third, and fourth locations respectively. Adapted from [Google Earth, 2013]

Another set of preliminary measurements was performed by RIVM along the A2 highway, slightly further south than the two stations mentioned previously. These measurements were taken on May 2nd 2024 at varying distance from the highway, near the Haarrijn service

station to the west of the road. A weak easterly wind (not measured directly) was observed during the measurements, so that each data series was acquired further downstream from the highway. Figure 13 shows the exact locations of the measurement device.

The table below shows the distances from the highway and the duration of the measurements, in chronological order. The first measurement began at 09:11 local time, and the last one finished at 11:24 local time.

Measurement details					
Location number	Coordinates	Perpendicular distance (m)	Downwind distance (m)	Number of samples	Wind dir. (deg)
1	N52°8′37.2″, E5°0′6.3″	60	60	35	70-40
2	N52°8′29.0″, E4°59′56.9″	320	400	29	40
3	N52°8′32.3″, E5°0′1.8″	200	270	12	40-80
4	N52°8′31.8″, E5°0′0.8″	220	300	31	80

Table 1: Details of the measurements taken near Haarrijn service station along the A2 highway. Locations are ordered chronologically, not by distance to the road. Both distance quantities are measured from the mobile measurement station, to the middle of the highway.

The reported wind directions are based on data measured at weather station De Bilt, roughly 13 km east-southeast, with wind speeds there decreasing from $5\,\mathrm{m\,s^{-1}}$ to $2\,\mathrm{m\,s^{-1}}$ while the preliminary data was collected. Traffic was observed to flow smoothly, with about 30% of vehicles being heavy goods vehicles (HGVs). The average distribution of particles of each data series is presented in the following figure.

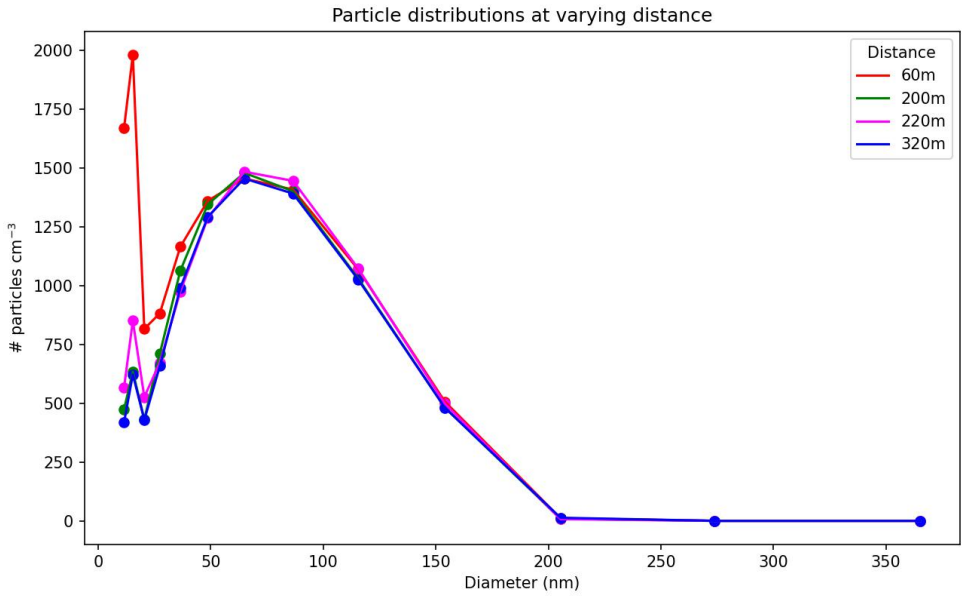

Figure 14: Particle distributions at varying distances from the A2 highway. Colours correspond to those of the markers in Figure 13. Data from [RIVM, 2024]

It is notable that there seems to be a large amount of particles below 20 nm diameter measured near the road, which very quickly disappear in the measurements further away from the road. at 60 m away, particle concentrations below 20 nm are around 4500 $\#/cm^3$, and after moving to roughly 270 m downwind from the highway, concentrations of particles below 20 nm decreased to between 1500 and 2000 $\#/cm^3$. Beyond that, for particles larger than roughly 50 nm, the distributions take roughly the same shape as one another, which we will call the local background. The distribution found at the distance of 60 m was used to initialise the model in the results presented in Section 4.1.1. To do this, the distribution had to be translated from the bins used by the SMPS device, to the bins used by SALSA2.0. The resulting distributions used by the model is presented in Figure 15 below.

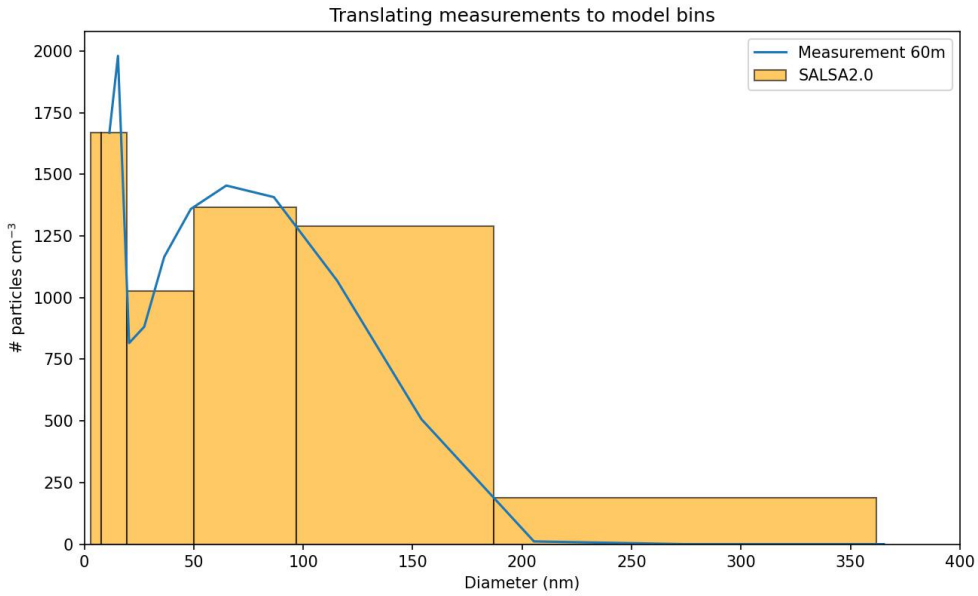

Figure 15: Initial particle distribution based on the measurement at 60 m from the highway at Haarrijn service station, translated to the SALSA2.0 model bins.

4 Results and discussion

4.1 Constant emissions

We performed multiple simulation runs with slightly different settings, specified when each set of results is presented. One set of simulations is performed using particle influx following a distribution characteristic of diesel emissions (see Figure 7), and another using a distribution more typical of gasoline emissions. Due to a lack of relevant measurements at multiple distances near highways, such as the preliminary series presented in Section 3.2, we are not able to validate the model's performance outright. The aim is to investigate the sensitivity to various parameters of our implementation of the model. The correlations shown in Figure 12, particularly those between particle counts, temperature and humidity, will be qualitatively confirmed.

4.1.1 Diesel emissions

We investigate our model's behaviour under diesel emissions, using a constant particle influx distribution as introduced in Section 3.1, with the model being initialised with the distribution measured at Haarrijn, 60 m from the highway. Environmental variables were tuned to be similar, so that $T = 293\,\mathrm{K}$, $RH = 67\%$ and $p = 99\,890\,\mathrm{Pa}$. The corresponding specific humidity the model uses is $q = 0.0097\,\mathrm{kg\,kg^{-1}}$.

The particle influx was scaled up to peak at around 10particles $\mathrm{cm^{-3}s^{-1}}$ for the bin spanning between roughly 96 and 187 nm. Dispersion rate was set to 1.2%.

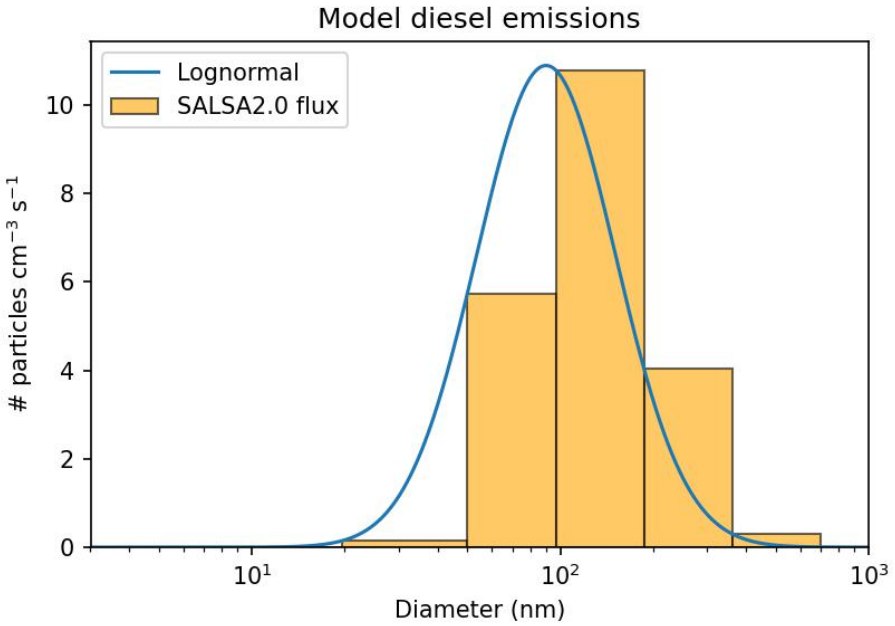

Figure 16: Influx of particles used in the model calculation (shown in orange), assumed to represent diesel emissions.

The results of this simulation are shown in the following figures. Both a distribution plot and a time series plot are given and compared to the preliminary Haarrijn measurement data where applicable.

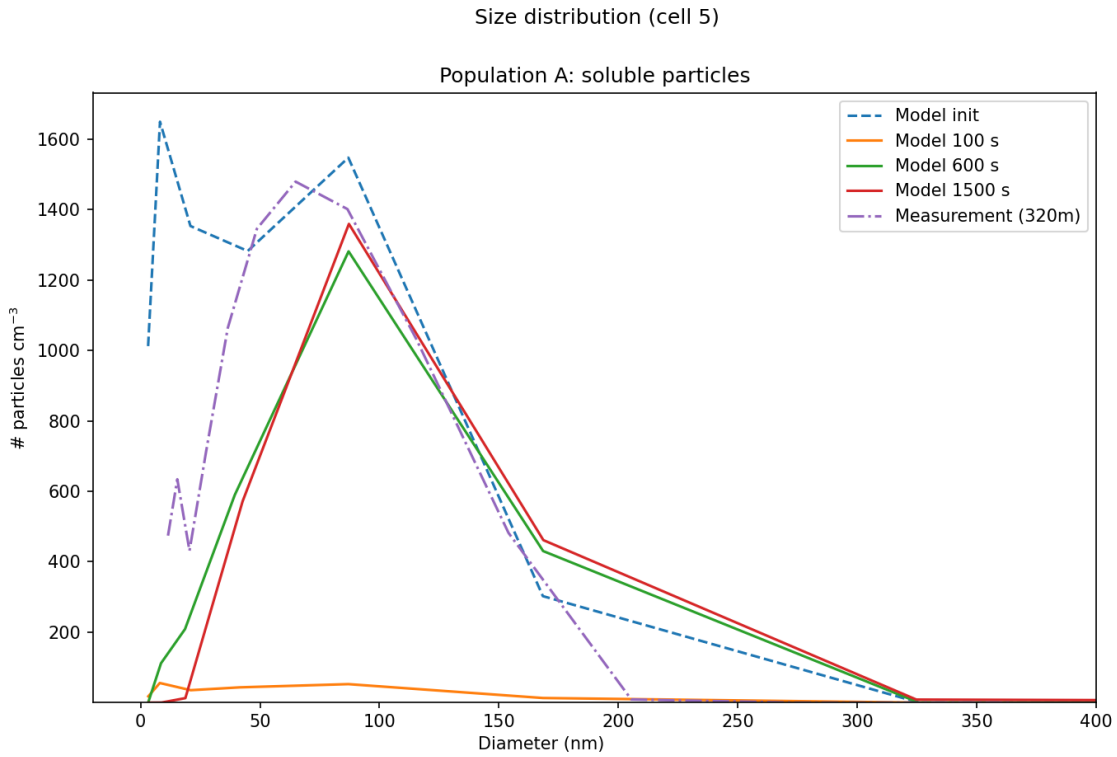

Figure 17: Plot of model particle distribution results in grid cell five at various times, with particle influx as found in diesel emissions. The blue dashed line shows the initial distribution of the first grid cell of the model. The three solid colour lines are the distribution as seen in grid cell five at the times listed in the legend. The purple dash-dotted line shows the particle distribution measured furthest away from the highway, at 320 m. The red and green vertical lines shown here correspond to the red and green lines in Figure 17.

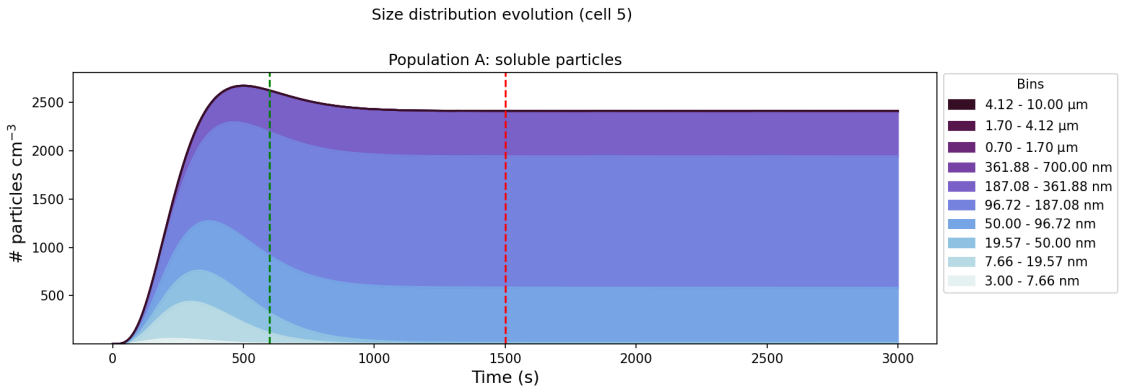

Figure 18: Stacked time series plot of model results in grid cell five with particle influx as found in diesel emissions. The different colours represent the particle numbers corresponding to the different particle size ranges (see legend). The green and red dashed lines correspond to the lines of the same colour in Figure 17.

Between these two figures, it can be seen that grid cell 5 starts out empty, and quickly grows in number, before reaching a peak at just before $t = 500\,\text{s}$. After this point, a stable balance seems to assert itself, with its peak around the diameter of 100 nm, which does not change much after $t = 1000\,\text{s}$, when most of the smallest particles have disappeared from the system. This is particularly obvious when viewing the time series plot, but can also be seen by the green (600 s) and red (1500 s) lines in Figure 17 not differing greatly. Similar to the measurements, modelled distributions seem to resemble the numbers found in the larger end of the distribution, where there are similar numbers of particles both close to and far away from the highway.

Additionally, compared to the measurement data (purple), there seem to be some particles missing in the smallest regime ($< 20\,\text{nm}$). The lack of these particles may be due to the model currently not simulating the formation of the secondary particles described earlier in Section 2.1. The exact number of particles to add in this way is difficult to determine a priori. In the scope of this investigation, this can be manually added to the influx of particles by adding another lognormal distribution with the same deviation to the diesel flux presented in Figure 16, with its peak on 20 nm, scaled to have its peak value half as high as the original diesel emissions distribution, resulting in a bimodal input distribution. Using this particle influx, the results do include particles in the smaller regimes.

It should be noted that the time after which a stable background remains is strongly dependent on the dispersion rate; a higher dispersion rate will result in the stable distribution asserting itself sooner. However, this means that the microphysical processes present in the model are increasingly overwhelmed by the dispersion mechanism, resulting in a stable distribution which becomes more identical to the constant flux distribution the higher the dispersion rate is.

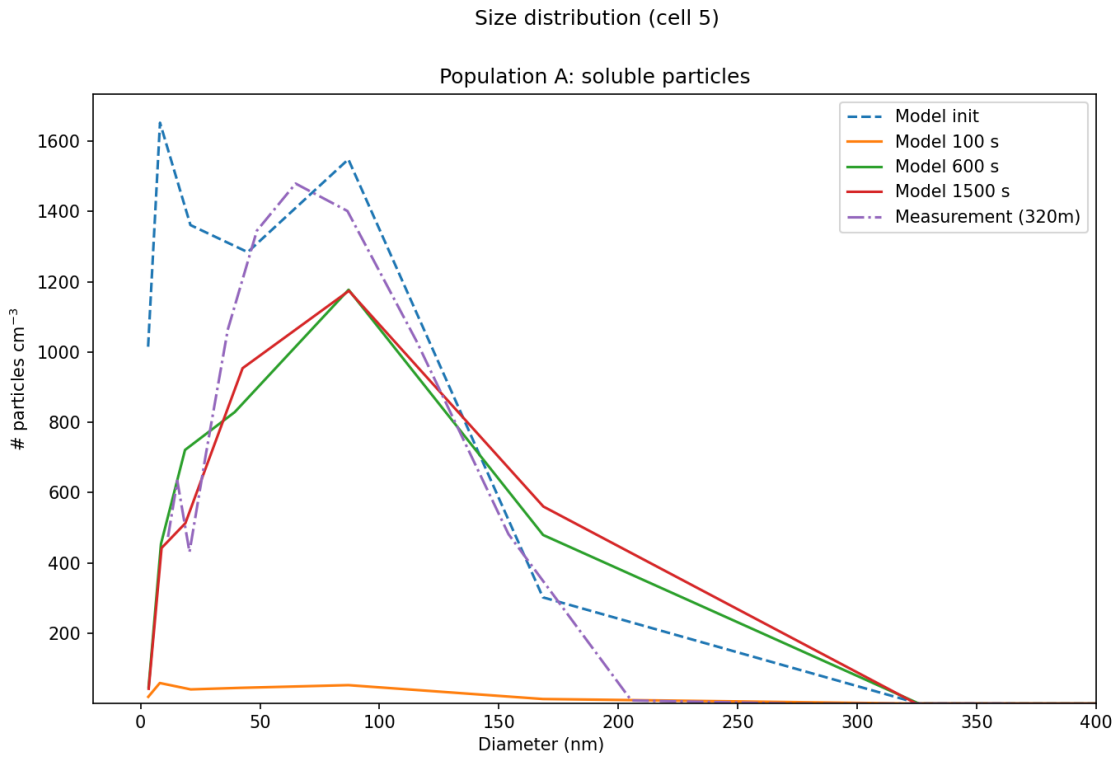

Figure 19: Similar to Figure 17: particle distribution plot of model results in grid cell five at various times, with additional particle influx in the smaller regime. This was done by adding a secondary lognormal distribution, with its peak at 20 nm, to the original influx distribution (Figure 16). The blue dashed line shows the initial distribution of the first grid cell of the model. The three solid colour lines are the distribution as seen in grid cell five at the times listed in the legend. The purple dash-dotted line shows the particle distribution measured furthest away from the highway, at 320 m.

With this input, there are still clearly particles present after 1500 s in the smaller regime, which is what was measured. However, the number of particles in the midrange, and particularly around the peak of the distribution, has now decreased, despite no change in that part of the input distribution or model settings. The tail of the distribution appears to have grown a little, suggesting that the extra influx of small particles has coagulated with the particles in the midrange to form larger particles. It should be noted that not all vehicles on the highway during the measurement series were diesel vehicles, so the weight given to this model finding should not be overestimated.

4.1.2 Gasoline emissions

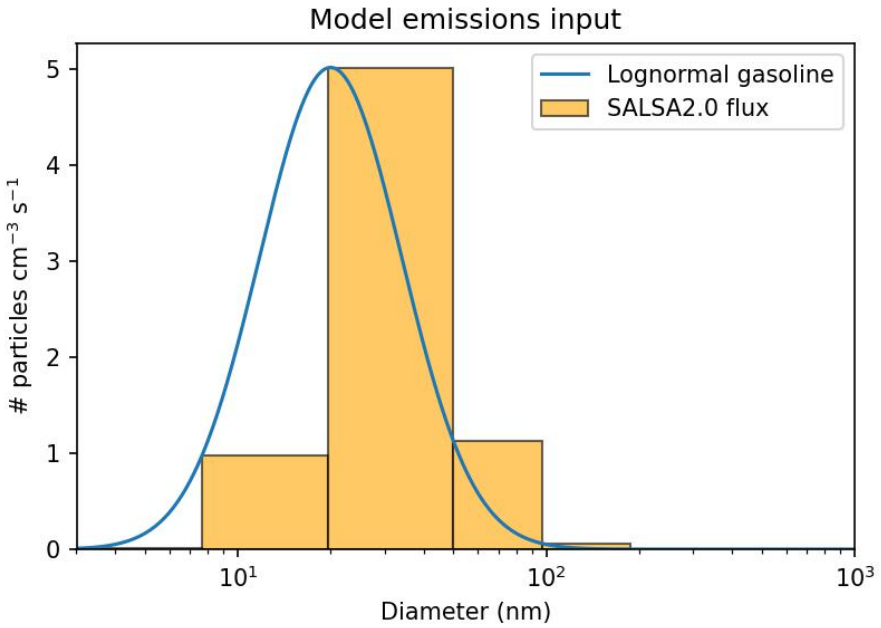

Figure 20: Lognormal curve (blue, based on Equation 1) describing gasoline particulate emissions, and corresponding model particle flux translated to bins used in SALSA2.0 (orange). Based on findings by [Huang et al., 2013].

The model was initialised with the distribution measured to the A2 highway, presented in Figure 15. We used a constant particle influx based on an approximation of the emissions found in gasoline vehicles, shown in Figure 20. Environmental variables were tuned to be similar, so that $T = 293\,\mathrm{K}$, $RH = 67\%$ and $p = 99\,890\,\mathrm{Pa}$. The corresponding specific humidity the model uses is $q = 0.0097\,\mathrm{kg\,kg^{-1}}$. The dispersion rate was set to 0.6% for this simulation. The results of this simulation are shown below, and compared to measurement data.

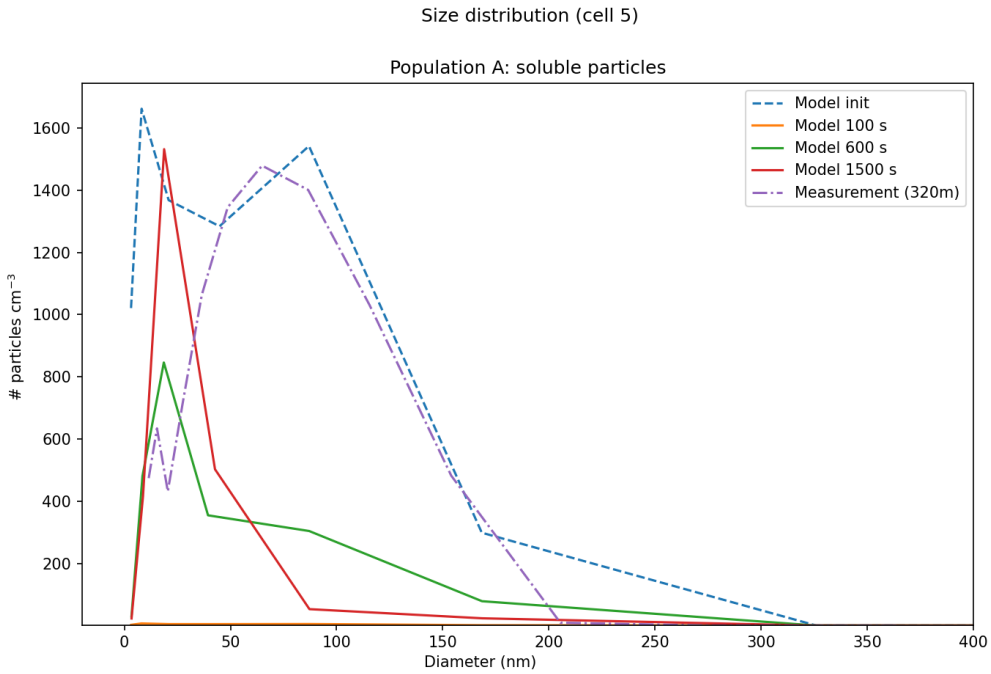

Figure 21: Plot of model particle distribution results in grid cell five at various times, with particle influx as found in gasoline emissions. The blue dashed line shows the initial distribution of the first grid cell of the model. The three solid colour lines are the distribution as seen in grid cell five at the times listed in the legend. The purple dash-dotted line shows the particle distribution measured furthest away from the highway, at 320 m. The red and green vertical lines shown here correspond to the red and green lines in Figure 22.

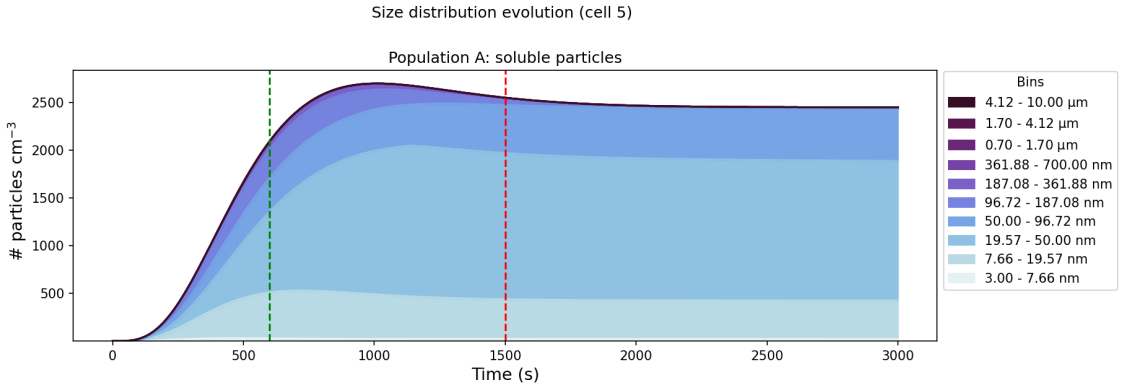

Figure 22: Stacked time series plot of model results in grid cell five with particle influx as found in gasoline emissions. The different colours represent the particle numbers corresponding to the different particle size ranges (see legend).

Given that gasoline emissions peak particularly strongly in the smaller regime, it is unsurprising to see this peak strongly in cell five after any amount of reacting. Though the model

was initialised with the Haarrijn data closest to the highway, there is no real resemblance between the measurement and the model data. Particles are lacking in the midrange and the end of the distribution of the model results. This is likely due to two factors. Foremost to the operation of this model, it is likely that larger particles are lacking due to them simply not being fed into the system by the constant influx of particles. Secondly, it may be the case that the mechanisms responsible for forming larger particles such as condensation and coagulation are overwhelmed by dispersive effects. This effect itself may be two-pronged. On the one hand, coagulation cannot occur (sufficiently quickly) when dispersion causes number concentrations to be relatively low. On the other hand, the dispersion rate may have been chosen in such a way, that the dynamic processes simply need more time to show significant effects. Decreasing the dispersion rate to allow the dynamic processes of the model more time to work, may remedy this issue. Section 4.2.2 goes into greater depth regarding our implementation of the model's sensitivity to dispersion.

It should be kept in mind that the only input currently given to the system, is those pertaining to engine emissions. However, in a real world scenario, the background concentration already present in the air would also be advected by wind or dispersed otherwise. This background concentration is usually characterised by increased numbers of particles in the midrange, particularly when close to highways. This background is currently missing from the input. In an attempt to add these to the system, additional particles are added into the fourth, fifth and sixth bins of the particle influx, according to the shape of the background measured at 320 m at Haarrijn service station, see Figure 14 (red line). The resultant shape of the input distribution is given in Figure 23 below.

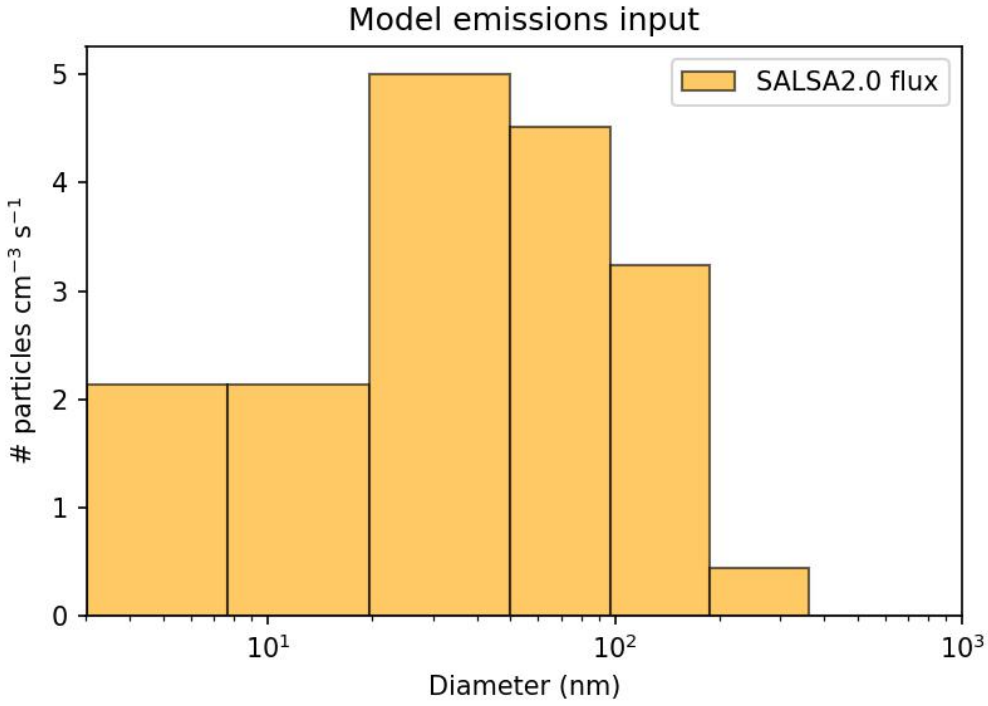

Figure 23: Similar to Figure 20 Influx of particles used in the model calculation, assumed to represent gasoline emissions, with additional emissions added based on background measurements.

Adding these additional particles into the system results, as expected, in an increase in particles particularly in the fourth and fifth bins. A very slight decrease of particles in the first two bins is observed as well.

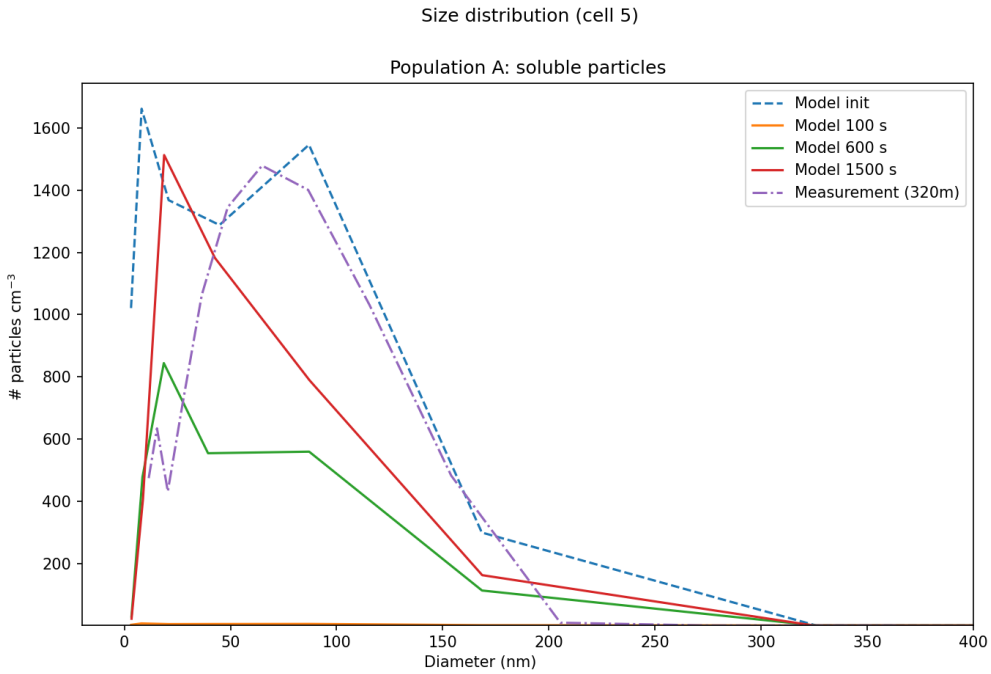

Figure 24: Plot of model particle distribution results in grid cell five at various times, with particle influx as found in gasoline emissions with additional input according to background measurements. The blue dashed line shows the initial distribution of the first grid cell of the model. The three solid colour lines are the distribution as seen in grid cell five at the times listed in the legend. The purple dash-dotted line shows the particle distribution measured furthest away from the highway, at 320 m. The red and green vertical lines shown here correspond to the red and green lines in Figure 25.

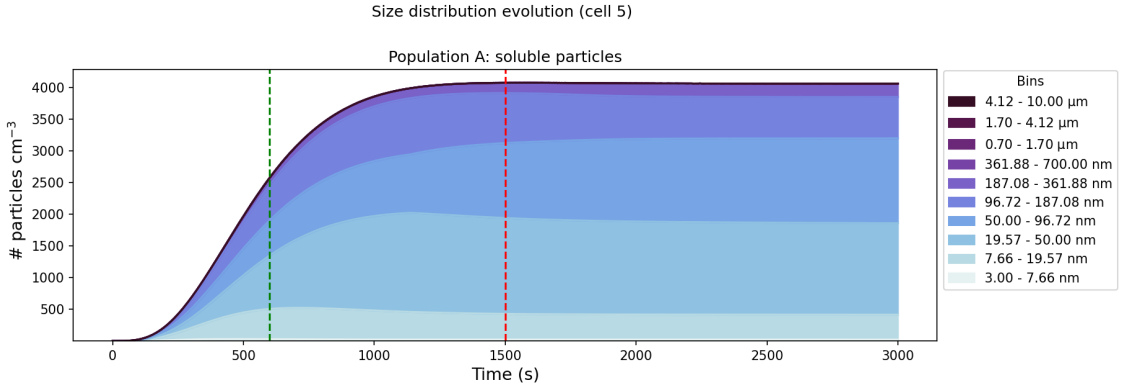

Figure 25: Stacked time series plot of model results in grid cell five with particle influx as found in gasoline emissions with additional input according to background measurements. The different colours represent the particle numbers corresponding to the different particle size ranges (see legend).

After $t = 1500\,\mathrm{s}$, when a stable balance seems to have mostly formed, there are still many more particles in the smaller regime, and not as many particles in the midrange, as was

measured at 320 m distance from the highway near Haarrijn service station. The excess of small particles is likely due to a relatively larger number of these being added constantly to the system, combined with dispersion not being strong enough to displace them. Adding particles into the midrange bins to simulate advected background concentrations like this, does not seem to be very effective.

4.2 Model sensitivity

We investigated the sensitivity of the model to various parameters, such as the environmental variables (temperature, specific humidity, and ambient pressure), as well as the parameters added to the model by our implementation of transport/dispersion. The shading of the 3-dimensional graphs is a function of the number of particles present at the time in the bin named at the top of the figure, to increase the legibility of the graphs. Section 4.2.1 presents the results of the sensitivity tests for the environmental variables, and Section 4.2.2 presents the results of the model to the dispersion rate d.

4.2.1 Environmental variables

The sensitivity of the model to environmental variables was investigated. Across these simulations, the initial distribution, particle influx and dispersion were kept the same. The initial distribution was set to the measurement at 60 m from the central axis of the highway near Haarrijn service station. The particle flux is the same bimodal distribution we used to model the additional secondary particle formation after diesel emissions used in the second run described in Section 4.1.1. Similarly, dispersion rate was set to 1.2%. Given that grid cell five starts out empty, the number of particles present after a certain amount of time is implicitly the difference between the starting point and the current time.

Firstly, we show the sensitivity of the model to changes in specific humidity and ambient temperature. We focus on the number of particles per bin after 1500 seconds of model time.

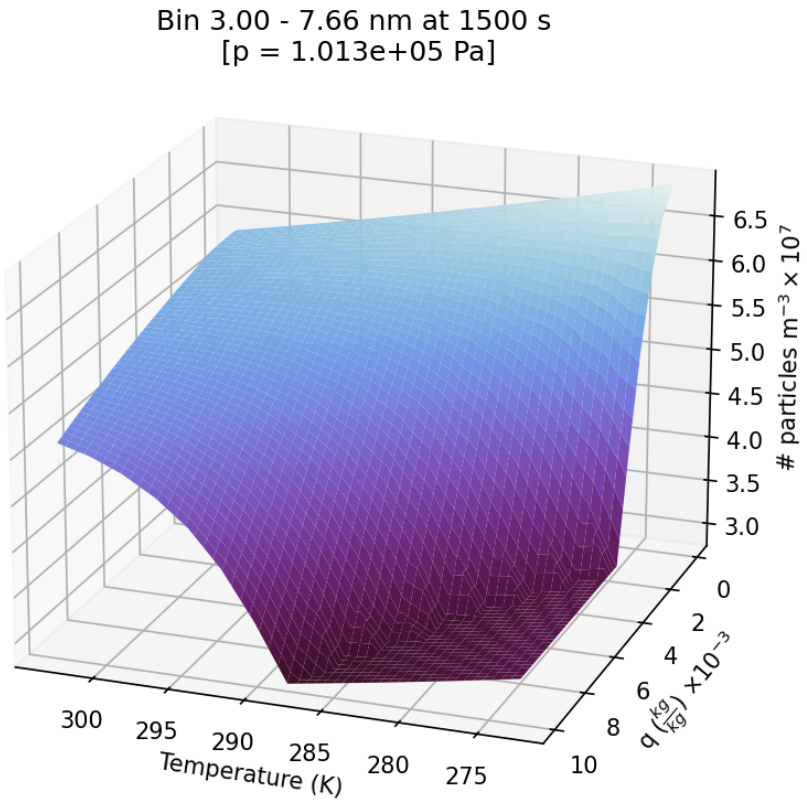

Figure 26: Surface plot of the number particles in grid cell 5 at 1500 s for varying temperature and specific humidity with a stable ambient pressure (see figure title). X-axis shows temperature, Y-axis shows specific humidity q, and the Z-axis shows the number of particles.

There seems to be a regime of low temperature and high specific humidity, where there are very little small particles left after 1500 s, roughly 30 #/cm^3. This number does not decrease further in time for these model runs. This small number is likely due to the relative humidity reaching 100% for these values of temperature and humidity, causing particles to stick together or to be lost due to wet deposition. Focusing on the higher values of humidity, there appears to be a positive relation with temperature - the higher the temperature, the higher the number of particles (about 1.5 particles cm^{-3} °C^{-1}), though this seems to tend asymptotically towards a maximum. Of course, the higher the temperature, the higher the average velocity of the particles. This facilitates the speed of the reactions producing new particles, but there may be a point at which the velocity of the particles is such, that coagulation processes outweigh these NPF processes, generating a maximum. In the portion with low specific humidity, there is a negative relation with temperature, unlike that in the region with higher humidity. All in all, both temperature and humidity seem to have a fairly strong effect on the particle concentration.

Looking back at the correlations shown in Section 3.2, we can see that there is not much

of a correlation between specific humidity or outside temperature and the smallest class of particles (labeled 11.5 in the correlation figures Figure 12). That is to say, it is likely that other variables, such as traffic intensity which was not measured, have a greater impact on the number of particles measured than humidity or temperature do. Despite this, we performed a linear regression between the measured (specific) humidity at NL1064 and number of particles in the smallest bin, and compared this to the same quantity in the model's results. The results of this linear regression are shown below in Figure 27. Similarly, a linear regression between ambient temperature and the number of particles in the smallest bin was calculated as measured at NL10641. The results of these are shown in Figure 28.

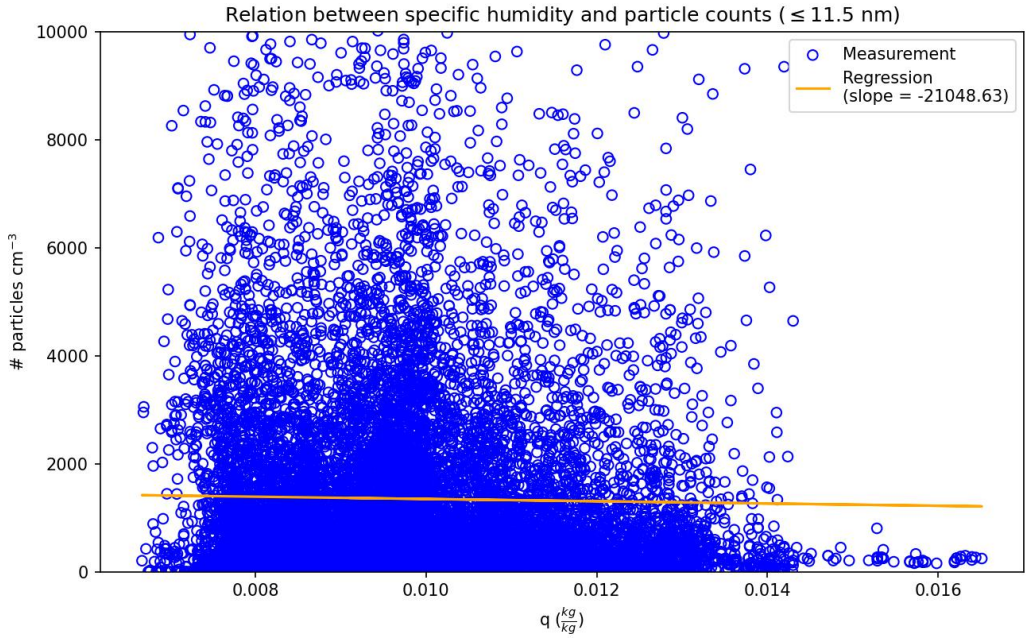

Figure 27: Scatter plot of the relation between specific humidity and particle number concentrations for the smallest size class, measured at NL10641 (location 1). The orange line shows a linear regression applied to the data. The Y-axis was limited at 10000 #/cm^3 to reduce visual skewing due to outliers.

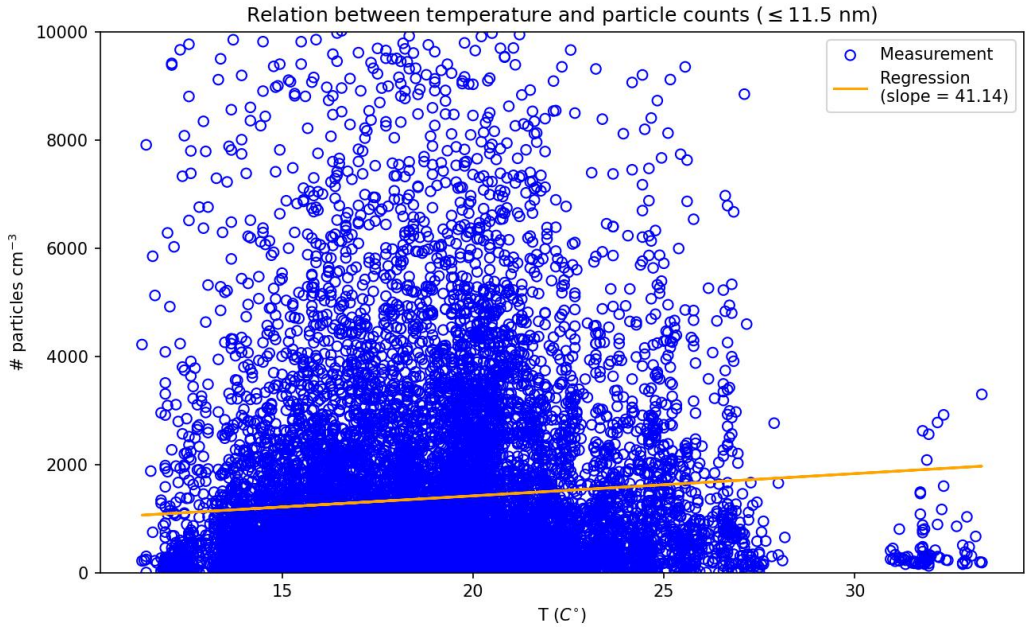

Figure 28: Scatter plot of the relation between ambient temperature and particle number concentrations for the smallest size class, measured at NL10641 (location 1). The orange line shows a linear regression applied to the data. The Y-axis was limited at 10000 #/cm^3 to reduce visual skewing due to outliers.

Both regressions qualitatively agree the corresponding findings in the model. We simulated a general negative relation (-752 particles cm^{-3} kg^{-1} for the highest temperature shown in Figure 29) between humidity and the smallest class of particles in SALSA, < 7.6 nm, which is also seen in the measurements (most clearly by the orange fit line) in Figure 27. This relation is seen more strongly in measurements, with a slope many times steeper. A general positive relation between temperature and particle counts is seen in the model, provided the specific humidity is not too low. This trend is also seen in measurements, although it is much stronger in the measurements at about 1.5 particles cm^{-3} °C^{-1} than in the simulation, at only about 1.5 particles cm^{-3} °C^{-1}. These correspondences lend credence to the model's applicability.

Secondly, we present the sensitivity to the model to changes in temperature and ambient pressure. The other conditions of the model were identical. The specific humidity was chosen so that relative humidity would not reach or exceed 100% anywhere in the range of temperatures and pressures used in the model runs.

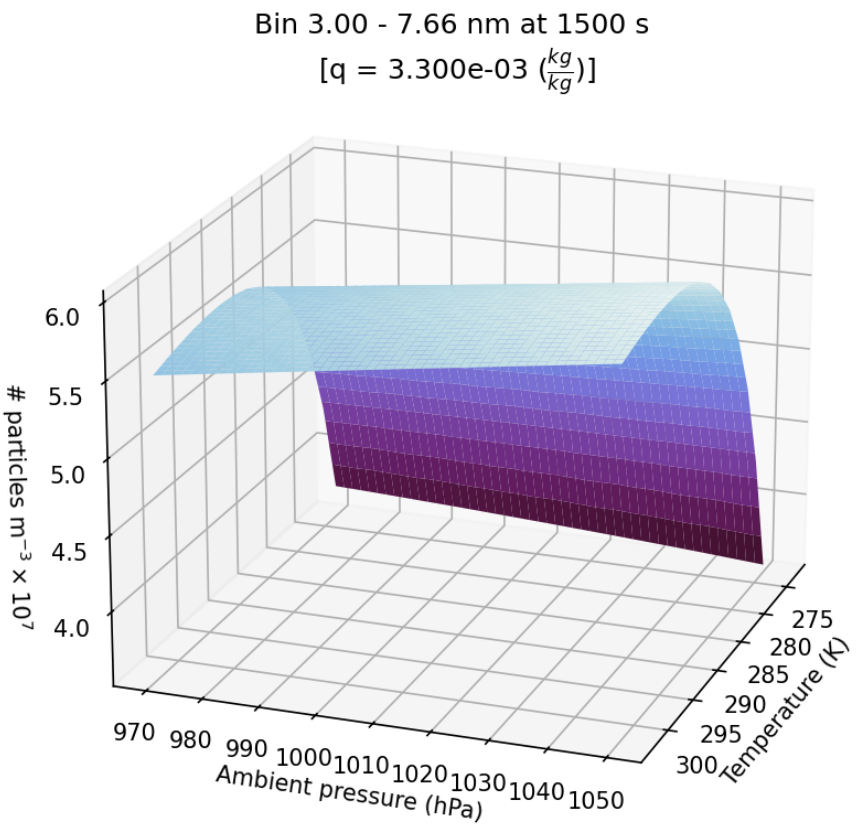

Figure 29: Surface plot of the particle number concentration for varying temperature and ambient pressure.

The relation with temperature shows a clear maximum for this specific humidity, which was alluded to in the previous subsection. There is a linear relation between air pressure and particle number, which is seen for all particle sizes, though only the smallest is presented here. The effect of air pressure is much weaker than that of humidity and temperature, with a small relative increase of roughly 5% over the range of pressures in the graph. This effect is not completely uncoupled from temperature, however, as a weak negative relation is seen for low temperatures, but a weak positive relation is seen for higher temperatures. The effect seems to be so insignificant (especially in the narrow range of ambient pressures encountered on the surface), that even finding relevant literature on the subject is difficult. This positive relation between ambient pressure was also found in the measurement data from station NL10641, though the low level of correlation as shown in Figure 12a indicate we should not take this relation too seriously. The figure below shows this relation for the measured data of NL10641, when the wind was coming from between SSW and NNW. Empty points were used to better visualise the relation. A subtle positive relation between air pressure and particle counts can be seen.

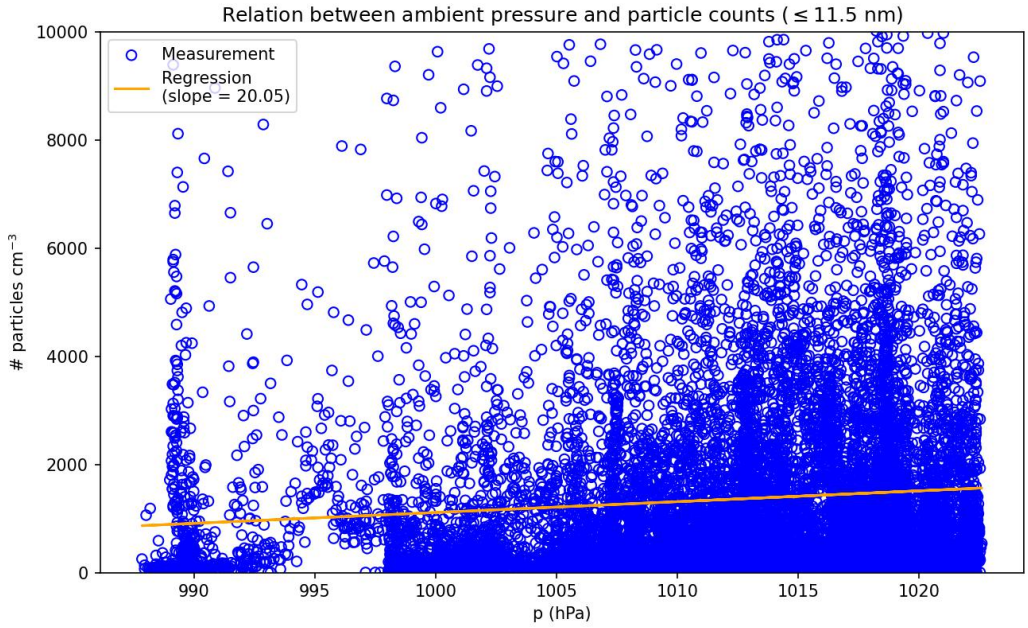

Figure 30: Scatter plot of the relation between ambient pressure and particle number concentrations for the smallest size class, measured at NL10641 (location 1). The orange line shows a linear regression applied to the data. The Y-axis was limited at 10000 #/cm^3 to reduce visual skewing due to outliers.

Comparing this graph's relation to that of the model's results for similar temperatures (291 K on average), the increase of particles of particles as calculated by the linear regression of the measurement data is stronger than that found in the model results (at about a 15% increase between $p = 988\,\text{hPa}$ and $p = 1023\,\text{hPa}$), but there may be a lot of confounding factors, such as traffic intensity, that limit the comparability of these two results.

4.2.2 Particle flux and dispersion

The sensitivity of the model to dispersion rate was investigated, given constant environmental variables ($T = 293\,\text{K}$, $RH = 67\%$ and $p = 99\,890\,\text{Pa}$). Grid cell one was initialised with the resampled distribution associated with wind directions coming from the highway near station NL10641, presented in Figure 11 (green line). It should be noted that this initialisation does not have a strong effect on the results presented here. Furthermore, the constant particle flux fed into grid cell one was the same as the one used in Section 4.1.1.

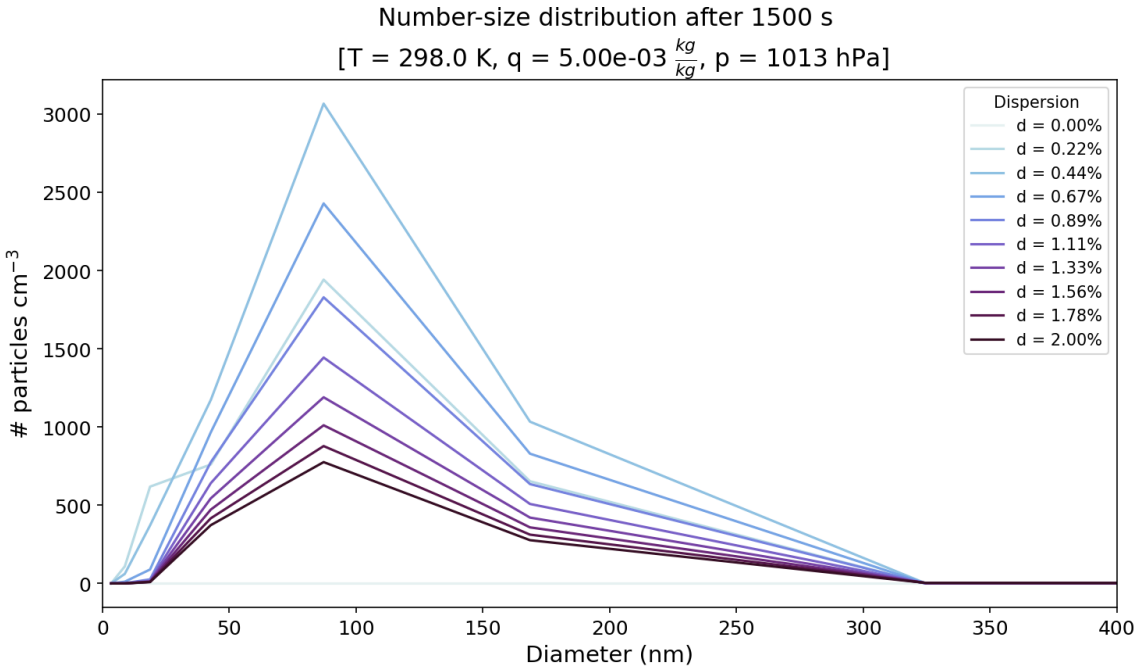

Figure 31: Particle distribution after 1500 seconds in grid cell five for various values of dispersion, where dispersion increases with darker line colours.

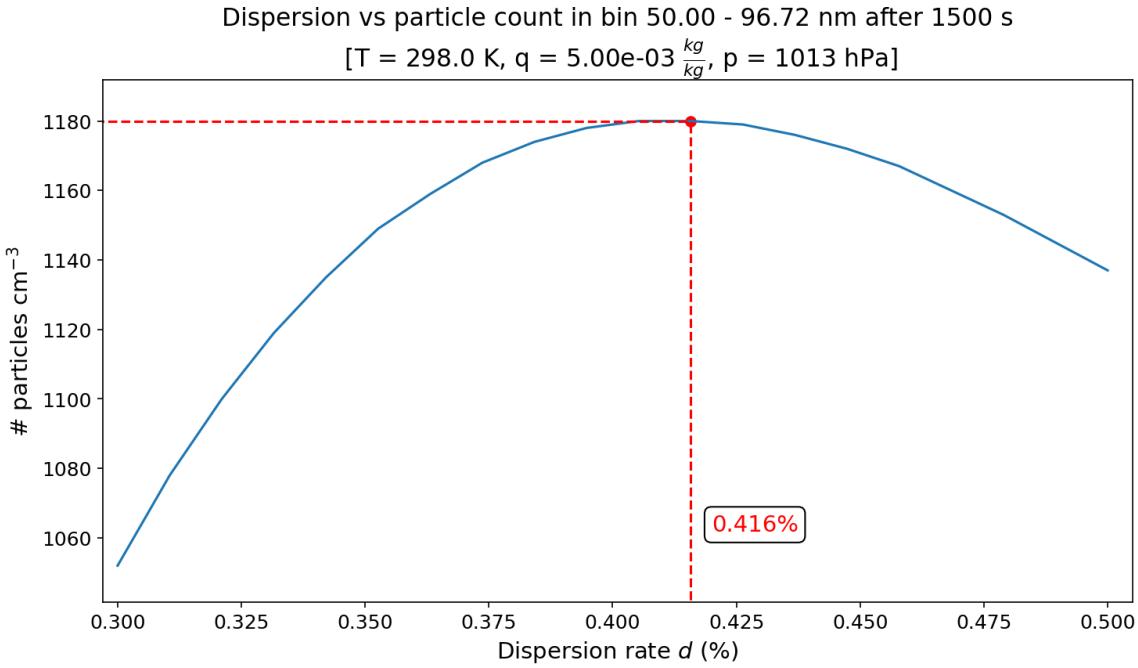

Figure 32: Relation between dispersion and the number of particles in one size bin 50 - 96.72 nm. The red dot and lines indicate the maximum particle count, with the red text stating the dispersion at which the maximum particle count is attained.

Building on the discussion started in Section 4.1.2 regarding the potentially non-linear effects of dispersion, we can see in Figure 31 zero dispersion (0%) results in no particles entering grid cell five, as expected. Increasing the dispersion increases the number of particles, but only up to a certain level of dispersion. It seems that somewhere between $d = 0.20\%$ and $d = 0.67\%$, the amount of particles reaches a maximum, after which an increase in dispersion is actually associated with a decrease of total number of particles for all bins. This has been investigated more closely by decreasing the step size between dispersion rates, and showing the relation between particle count and dispersion directly in Figure 32. The dispersion rate at which this maximum is achieved, was found to be at $d = 0.416\%$, though it must be noted that this will likely be dependent on the environmental factors and the constant particle influx distribution as well. This result lends credence to the idea that the dispersion rate has a more complicated effect on the model's output than just increasing or decreasing all particle counts, but has an interaction with the chemical and microphysics schemes present in the model. The stronger the dispersive effects are, the more they will overwhelm the microphysical processes present in the model.

5 Discussion and conclusions

In this thesis, we investigated the behaviour of UFPs on short timescales near a highway with constant particle emissions, as modelled in a modified version of the HAM/SALSA2.0 box model, and as measured near a highway. It was found that particles in the smallest regime (< 20 nm) disappear quickly as the measurement distance from the highway increases, while particles of greater size seemed mostly constant regardless of distance. After moving to roughly 270 m downwind from the highway, concentrations of particles below 20 nm were between 1500 and 2000 #/cm^3, down from roughly 4500 #/cm^3 at 60 m away. At a greater distance of 400 m downwind, the particle distribution did not change much as compared to at 270 m; a stable background seemed to remain. A study done by Zhu et al. [2002] with similar measurements, found an even stronger decrease in particle concentration. It must be noted that the highway next to which their measurements were performed might have been busier, resulting in larger particle counts close to the road. By implementing dispersion and a constant source of particles, we were able to determine how quickly a stable particle distribution appears in our model after initialisation. In the range of values used for the dispersion rate d, between 0.6% and 1.2%, the resultant particle distributions had mostly reached their stable configuration after 1000 s, and were fully stable after 1500 s. Additionally, we set out to study the sensitivity of our model to humidity and temperature, and these were confirmed to qualitatively correspond to trends in measurements. Depending on temperature, our model showed a negative relation between specific humidity and concentration of particles below 20 nm of -752 particles cm^{-3} kg^{-1} at 303 K, which was also tentatively present (although stronger) in measurements. Stronger but similar correlations were found by Sabaliauskas et al. [2012] in a five-year roadside measurement in a major Canadian city. Furthermore, our model exhibits a positive relation between temperature and particle concentration of about 1.5 particles cm^{-3} °C^{-1}, in the most humid regime tested. This general positive trend becomes weaker for lower humidity. Similar relations between these meteorological variables and particle concentrations for urban environments have been found before by Wang et al. [2011]. Additionally, a very weak relation between air pressure and particle concentration was also identified in the model, which was not completely independent of temperature. For higher temperatures (303 K), this meant a 5% increase in concentrations of particles between 3 nm and 7.66 nm as pressure increased from 988 hPa to 1023 hPa. Again, a similar but stronger relation was seen in measurements. While it is known that air pressure can have an effect on particle counts through condensation and coagulation, it isn't trivial to quantify this effect [Seigneur, 2019]. Finally, we wanted to study our model's dependence on its dispersion rate parameter d. We saw that there is a non-linear relationship between particle counts and dispersion, indicating a more complex interaction than simply locally removing particles. We found that, given a certain particle influx distribution, the stable concentration (after 1500 s) of particles between 50 and 96.72 nm reached a maximum for $d = 0.416\%$.

While our study provides a useful model to simulate the effects of different emissions profiles and dispersion on a resulting background distribution, it has some limitations. The primary one is the difficulty in relating the effects of dispersion to any real-world parameter such as wind speed or atmospheric stability, or even a simple distance. This makes it challenging to compare the model's results to measurements. This is largely inherent to the 0-dimensional nature of this model. A study by Nikolova et al. [2011] investigated the dispersion of UFP in

an urban street canyon using the 3D CFD model ENVI-met®. While not strictly the same as our modelled scenario or the same scale, they were able to reproduce the spatial distribution of UFP well. Kurppa et al. [2019] implemented the SALSA2.0 model into the large-eddy simulation (LES) model PALM to model UFP dispersion in an urban street canyon, with good results. These models are both able to simulate dispersion around physical obstructions such as buildings, and may be more fit to simulate future work. The lack of a possibility to simulate the formation of secondary particles from gaseous vehicle emissions in our model currently needs to be compensated for by manually adapting the emissions profiles, limiting the model's completeness. Furthermore, the main measurement series of interest presented in this thesis was preliminary, which means we cannot rely on its implications too much.

Building on our findings, a few suggestions for future work emerge. The model currently uses the same dispersion rate d throughout, implying that every particle leaving one grid cell travels to the adjacent cell. Decoupling the dispersion rate into an incoming and outgoing rate may prove useful, and simulates the possibility of particles "exiting" the model system altogether. Additionally, an assumption regarding the mass mixing ratio of the aerosol particles was made in the initialisation of the model. For example, it assumes that 80% of the mass of the smallest particle class consists of organic carbon. Tuning these mixing ratios to be as close to measurements as possible may make the model's results more realistic as well. Furthermore, expressing this dispersion rate in terms of real-world parameters such as atmospheric stability is crucial to relating the model's results to measurement data. Either describing dispersion in terms of atmospheric stability, or by measuring a stable tracer such as NO_x at varying distances from a source to determine its dispersion, can help dispersion rates take more realistic values, and increase the model's applicability. Finally, more particle distribution measurements at varying distances from a source are crucial to broaden our understanding of UFP behaviour near busy roads.

References

A. A. Abdel-Rahman. On the atmospheric dispersion and gaussian plume model. In *Proceedings of the 2nd International Conference on Waste Management, Water Pollution, Air Pollution, Indoor Climate, Corfu, Greece*, volume 26, 2008.

H. I. Abdel-Shafy and M. S. Mansour. A review on polycyclic aromatic hydrocarbons: Source, environmental impact, effect on human health and remediation. *Egyptian Journal of Petroleum*, 25(1):107–123, 2016. ISSN 1110-0621. doi: https://doi.org/10.1016/j.ejpe.2015.03.011. URL https://www.sciencedirect.com/science/article/pii/S1110062114200237.

S. F. Abdillah and Y.-F. Wang. Ambient ultrafine particle (pm0.1): Sources, characteristics, measurements and exposure implications on human health. *Environmental Research*, 218: 115061, 2023. ISSN 0013-9351. doi: https://doi.org/10.1016/j.envres.2022.115061. URL https://www.sciencedirect.com/science/article/pii/S001393512202388X.

A. Y. Bigazzi and M. A. Figliozzi. Impacts of freeway traffic conditions on in-vehicle exposure to ultrafine particulate matter. *Atmospheric Environment*, 60:495–503, 2012. ISSN 1352-2310. doi: https://doi.org/10.1016/j.atmosenv.2012.07.020. URL https://www.sciencedirect.com/science/article/pii/S1352231012006929.

G. R. Cass, L. A. Hughes, P. Bhave, M. J. Kleeman, J. O. Allen, and L. G. Salmon. The chemical composition of atmospheric ultrafine particles. *Philosophical Transactions of the Royal Society of London. Series A: Mathematical, Physical and Engineering Sciences*, 358(1775):2581–2592, Oct. 2000. ISSN 1471-2962. doi: 10.1098/rsta.2000.0670. URL http://dx.doi.org/10.1098/rsta.2000.0670.

A. Charron and R. M. Harrison. Primary particle formation from vehicle emissions during exhaust dilution in the roadside atmosphere. *Atmospheric Environment*, 37(29):4109–4119, 2003. ISSN 1352-2310. doi: https://doi.org/10.1016/S1352-2310(03)00510-7. URL https://www.sciencedirect.com/science/article/pii/S1352231003005107.

M. Chatain, R. Alvarez, A. Ustache, E. Rivière, O. Favez, and C. Pallares. Simultaneous roadside and urban background measurements of submicron aerosol number concentration and size distribution (in the range 20–800 nm), along with chemical composition in strasbourg, france. *Atmosphere*, 12(1), 2021. ISSN 2073-4433. doi: 10.3390/atmos12010071. URL https://www.mdpi.com/2073-4433/12/1/71.

W. Choi, S. Hu, M. He, K. Kozawa, S. Mara, A. M. Winer, and S. E. Paulson. Neighborhood-scale air quality impacts of emissions from motor vehicles and aircraft. *Atmospheric Environment*, 80:310–321, 2013. ISSN 1352-2310. doi: https://doi.org/10.1016/j.atmosenv.2013.07.043. URL https://www.sciencedirect.com/science/article/pii/S1352231013005724.

J. Curtius. Nucleation of atmospheric aerosol particles. *Comptes Rendus Physique*, 7(9):1027–1045, 2006. ISSN 1631-0705. doi: https://doi.org/10.1016/j.crhy.2006.10.018. URL https://www.sciencedirect.com/science/article/pii/S1631070506002301. Nucleation.

L. Dada, D. Stolzenburg, M. Simon, L. Fischer, M. Heinritzi, M. Wang, M. Xiao, A. L. Vogel, L. Ahonen, A. Amorim, R. Baalbaki, A. Baccarini, U. Baltensperger, F. Bianchi, K. R. Daellenbach, J. DeVivo, A. Dias, J. Dommen, J. Duplissy, H. Finkenzeller, A. Hansel, X.-C. He, V. Hofbauer, C. R. Hoyle, J. Kangasluoma, C. Kim, A. Kürten, A. Kvashnin, R. Mauldin, V. Makhmutov, R. Marten, B. Mentler, W. Nie, T. Petäjä, L. L. J. Quéléver, H. Saathoff, C. Tauber, A. Tome, U. Molteni, R. Volkamer, R. Wagner, A. C. Wagner, D. Wimmer, P. M. Winkler, C. Yan, Q. Zha, M. Rissanen, H. Gordon, J. Curtius, D. R. Worsnop, K. Lehtipalo, N. M. Donahue, J. Kirkby, I. E. Haddad, and M. Kulmala. Role of sesquiterpenes in biogenic new particle formation. *Science Advances*, 9(36):eadi5297, 2023. doi: 10.1126/sciadv.adi5297. URL `https://www.science.org/doi/abs/10.1126/sciadv.adi5297`.

A. L. de Jesus, M. M. Rahman, M. Mazaheri, H. Thompson, L. D. Knibbs, C. Jeong, G. Evans, W. Nei, A. Ding, L. Qiao, L. Li, H. Portin, J. V. Niemi, H. Timonen, K. Luoma, T. Petäjä, M. Kulmala, M. Kowalski, A. Peters, J. Cyrys, L. Ferrero, M. Manigrasso, P. Avino, G. Buonano, C. Reche, X. Querol, D. Beddows, R. M. Harrison, M. H. Sowlat, C. Sioutas, and L. Morawska. Ultrafine particles and pm2.5 in the air of cities around the world: Are they representative of each other? *Environment International*, 129: 118–135, 2019. ISSN 0160-4120. doi: https://doi.org/10.1016/j.envint.2019.05.021. URL `https://www.sciencedirect.com/science/article/pii/S0160412019311110`.

C. L. Dias, M. L. Oliveira, J. C. Hower, S. R. Taffarel, R. M. Kautzmann, and L. F. Silva. Nanominerals and ultrafine particles from coal fires from santa catarina, south brazil. *International Journal of Coal Geology*, 122:50–60, 2014. ISSN 0166-5162. doi: https://doi.org/10.1016/j.coal.2013.12.011. URL `https://www.sciencedirect.com/science/article/pii/S0166516213002784`.

M. Ehn, J. A. Thornton, E. Kleist, M. Sipilä, H. Junninen, I. Pullinen, M. Springer, F. Rubach, R. Tillmann, B. Lee, F. Lopez-Hilfiker, S. Andres, I.-H. Acir, M. Rissanen, T. Jokinen, S. Schobesberger, J. Kangasluoma, J. Kontkanen, T. Nieminen, T. Kurtén, L. B. Nielsen, S. Jørgensen, H. G. Kjaergaard, M. Canagaratna, M. D. Maso, T. Berndt, T. Petäjä, A. Wahner, V.-M. Kerminen, M. Kulmala, D. R. Worsnop, J. Wildt, and T. F. Mentel. A large source of low-volatility secondary organic aerosol. *Nature*, 506 (7489):476–479, Feb. 2014. ISSN 1476-4687. doi: 10.1038/nature13032. URL `http://dx.doi.org/10.1038/nature13032`.

EukerAlert.org. Brief exposure to tiny air pollution particles triggers childhood lung infections. URL `https://www.eurekalert.org/multimedia/601276`. [Accessed 17-06-2024].

S. Fruin, D. Westerdahl, T. Sax, C. Sioutas, and P. Fine. Measurements and predictors of on-road ultrafine particle concentrations and associated pollutants in los angeles. *Atmospheric Environment*, 42(2):207–219, 2008. ISSN 1352-2310. doi: https://doi.org/10.1016/j.atmosenv.2007.09.057. URL `https://www.sciencedirect.com/science/article/pii/S135223100700859X`.

Gezondheidsraad. Achtergronddocument gezondheidseffecten ultrafijnstof, 9 2021.

URL https://www.gezondheidsraad.nl/documenten/adviezen/2021/09/15/risicos-van-ultrafijnstof-in-de-buitenlucht.

Google Earth. Google earth v 10.52.0.0. the netherlands, europe. 52° 15' 10"n 5° 05' 35"e, eye alt 264km. http://www.earth.google.com, April 2013. [Accessed 15-04-2024].

S. J. Harris and M. Maricq. Signature size distributions for diesel and gasoline engine exhaust particulate matter. *Journal of Aerosol Science*, 32(6):749–764, 2001. ISSN 0021-8502. doi: https://doi.org/10.1016/S0021-8502(00)00111-7. URL https://www.sciencedirect.com/science/article/pii/S0021850200001117.

J. Hofman, J. Staelens, R. Cordell, C. Stroobants, N. Zikova, S. Hama, K. Wyche, G. Kos, S. Van Der Zee, K. Smallbone, E. Weijers, P. Monks, and E. Roekens. Ultrafine particles in four european urban environments: Results from a new continuous long-term monitoring network. *Atmospheric Environment*, 136:68–81, 2016. ISSN 1352-2310. doi: https://doi.org/10.1016/j.atmosenv.2016.04.010. URL https://www.sciencedirect.com/science/article/pii/S1352231016302783.

C. Huang, D. Lou, Z. Hu, Q. Feng, Y. Chen, C. Chen, P. Tan, and D. Yao. A pems study of the emissions of gaseous pollutants and ultrafine particles from gasoline- and diesel-fueled vehicles. *Atmospheric Environment*, 77:703–710, 2013. ISSN 1352-2310. doi: https://doi.org/10.1016/j.atmosenv.2013.05.059. URL https://www.sciencedirect.com/science/article/pii/S1352231013004238.

J. I. Huertas, D. S. Martinez, and D. F. Prato. Numerical approximation to the effects of the atmospheric stability conditions on the dispersion of pollutants over flat areas. *Scientific Reports*, 11(1), June 2021. ISSN 2045-2322. doi: 10.1038/s41598-021-89200-9. URL http://dx.doi.org/10.1038/s41598-021-89200-9.

N. Janssen, D. Houthuijs, and A. Dusseldorp. Gezondheidseffecten van ultrafijn stof van vliegverkeer rond schiphol, 2022. URL https://rivm.openrepository.com/handle/10029/625853.

J. Kammer, P.-M. Flaud, A. Chazeaubeny, R. Ciuraru, K. Le Menach, E. Geneste, H. Budzinski, J. Bonnefond, E. Lamaud, E. Perraudin, and E. Villenave. Biogenic volatile organic compounds (bvocs) reactivity related to new particle formation (npf) over the landes forest. *Atmospheric Research*, 237:104869, 2020. ISSN 0169-8095. doi: https://doi.org/10.1016/j.atmosres.2020.104869. URL https://www.sciencedirect.com/science/article/pii/S0169809519312980.

L. D. Knibbs and R. J. de Dear. Exposure to ultrafine particles and pm2.5 in four sydney transport modes. *Atmospheric Environment*, 44(26):3224–3227, 2010. ISSN 1352-2310. doi: https://doi.org/10.1016/j.atmosenv.2010.05.026. URL https://www.sciencedirect.com/science/article/pii/S1352231010003997.

H. Kokkola, T. Kühn, A. Laakso, T. Bergman, K. E. J. Lehtinen, T. Mielonen, A. Arola, S. Stadtler, H. Korhonen, S. Ferrachat, U. Lohmann, D. Neubauer, I. Tegen, C. Siegenthaler-Le Drian, M. G. Schultz, I. Bey, P. Stier, N. Daskalakis, C. L. Heald, and

S. Romakkaniemi. Salsa2.0: The sectional aerosol module of the aerosol–chemistry–climate model echam6.3.0-ham2.3-moz1.0. *Geoscientific Model Development*, 11(9):3833–3863, 2018. doi: 10.5194/gmd-11-3833-2018. URL https://gmd.copernicus.org/articles/11/3833/2018/.

T. Kuhn, M. Krudysz, Y. Zhu, P. M. Fine, W. C. Hinds, J. Froines, and C. Sioutas. Volatility of indoor and outdoor ultrafine particulate matter near a freeway. *Journal of Aerosol Science*, 36(3):291–302, 2005. ISSN 0021-8502. doi: https://doi.org/10.1016/j.jaerosci.2004.09.006. URL https://www.sciencedirect.com/science/article/pii/S0021850204003428.

M. Kurppa, A. Hellsten, P. Roldin, H. Kokkola, J. Tonttila, M. Auvinen, C. Kent, P. Kumar, B. Maronga, and L. Järvi. Implementation of the sectional aerosol module salsa2.0 into the palm model system 6.0: model development and first evaluation. *Geoscientific Model Development*, 12(4):1403–1422, 2019. doi: 10.5194/gmd-12-1403-2019. URL https://gmd.copernicus.org/articles/12/1403/2019/.

H.-S. Kwon, M. H. Ryu, and C. Carlsten. Ultrafine particles: unique physicochemical properties relevant to health and disease. *Experimental amp; Molecular Medicine*, 52(3):318–328, Mar. 2020. ISSN 2092-6413. doi: 10.1038/s12276-020-0405-1. URL http://dx.doi.org/10.1038/s12276-020-0405-1.

N. Li, S. Georas, N. Alexis, P. Fritz, T. Xia, M. A. Williams, E. Horner, and A. Nel. A work group report on ultrafine particles (american academy of allergy, asthma immunology): Why ambient ultrafine and engineered nanoparticles should receive special attention for possible adverse health outcomes in human subjects. *Journal of Allergy and Clinical Immunology*, 138(2):386–396, 2016. ISSN 0091-6749. doi: https://doi.org/10.1016/j.jaci.2016.02.023. URL https://www.sciencedirect.com/science/article/pii/S0091674916300112.

L. Morawska, Z. Ristovski, E. Jayaratne, D. Keogh, and X. Ling. Ambient nano and ultrafine particles from motor vehicle emissions: Characteristics, ambient processing and implications on human exposure. *Atmospheric Environment*, 42(35):8113–8138, 2008. ISSN 1352-2310. doi: https://doi.org/10.1016/j.atmosenv.2008.07.050. URL https://www.sciencedirect.com/science/article/pii/S1352231008006961.

A. L. Moreno-Ríos, L. P. Tejeda-Benítez, and C. F. Bustillo-Lecompte. Sources, characteristics, toxicity, and control of ultrafine particles: An overview. *Geoscience Frontiers*, 13 (1):101147, 2022. ISSN 1674-9871. doi: https://doi.org/10.1016/j.gsf.2021.101147. URL https://www.sciencedirect.com/science/article/pii/S1674987121000116.

A. Mukherjee and M. Agrawal. World air particulate matter: sources, distribution and health effects. *Environmental Chemistry Letters*, 15(2):283–309, Feb. 2017. ISSN 1610-3661. doi: 10.1007/s10311-017-0611-9. URL http://dx.doi.org/10.1007/s10311-017-0611-9.

R. C. Muñoz and M. J. Corral. Surface indices of wind, stability, and turbulence at a highly polluted urban site in santiago, chile, and their relationship with nocturnal particulate

matter concentrations. *Aerosol and Air Quality Research*, 17(11):2780–2790, 2017. ISSN 2071-1409. doi: 10.4209/aaqr.2017.05.0190. URL http://dx.doi.org/10.4209/aaqr.2017.05.0190.

S. S. Nadadur and J. W. Hollingsworth, editors. *Air Pollution and Health Effects*. Molecular and Integrative Toxicology. Springer, London, England, 2015 edition, May 2015.

I. Nikolova, S. Janssen, P. Vos, K. Vrancken, V. Mishra, and P. Berghmans. Dispersion modelling of traffic induced ultrafine particles in a street canyon in antwerp, belgium and comparison with observations. *Science of The Total Environment*, 412-413:336–343, 2011. ISSN 0048-9697. doi: https://doi.org/10.1016/j.scitotenv.2011.09.081. URL https://www.sciencedirect.com/science/article/pii/S0048969711011156.

L. Ntziachristos, Z. Ning, M. D. Geller, and C. Sioutas. Particle concentration and characteristics near a major freeway with heavy-duty diesel traffic. *Environmental Science & Technology*, 41(7):2223–2230, 2007. doi: 10.1021/es062590s. URL https://doi.org/10.1021/es062590s. PMID: 17438767.

S. N. Pandis and J. H. Seinfeld. *Atmospheric Chemistry and Physics: From Air Pollution to Climate Change*. John Wiley Sons, Incorporated, Newark, 3 edition, May 2016. doi: 978-1-118-94740-1.

PNNL. Scientists more accurately model the formation and growth of tiny particles that influence clouds and climate — phys.org. https://phys.org/news/2016-03-scientists-accurately-formation-growth-tiny.html, March 2016. [Accessed 06-06-2024].

M. Pohjola, L. Pirjola, J. Kukkonen, and M. Kulmala. Correction to modelling of the influence of aerosol processes for the dispersion of vehicular exhaust plumes in street environment. *Atmospheric Environment*, 40(2):311–314, 2006. ISSN 1352-2310. doi: https://doi.org/10.1016/j.atmosenv.2005.09.039. URL https://www.sciencedirect.com/science/article/pii/S135223100500885X.

F. Prodi and F. Tampieri. The removal of particulate matter from the atmosphere: the physical mechanisms. *Pure and Applied Geophysics PAGEOPH*, 120(2):286–325, 1982. ISSN 1420-9136. doi: 10.1007/bf00877038. URL http://dx.doi.org/10.1007/BF00877038.

P. Quincey and D. Butterfield. Ambient air particulate matter pm10and pm2.5: developments in european measurement methods and legislation. *Biomarkers*, 14(sup1):34–38, July 2009. ISSN 1366-5804. doi: 10.1080/13547500902965484. URL http://dx.doi.org/10.1080/13547500902965484.

D. Rim, M. Green, L. Wallace, A. Persily, and J.-I. Choi. Evolution of ultrafine particle size distributions following indoor episodic releases: Relative importance of coagulation, deposition and ventilation. *Aerosol Science and Technology*, 46(5):494–503, May 2012. ISSN 1521-7388. doi: 10.1080/02786826.2011.639317. URL http://dx.doi.org/10.1080/02786826.2011.639317.

RIVM. Normen luchtkwaliteit. https://www.rijksoverheid.nl/onderwerpen/luchtkwaliteit/normen-luchtkwaliteit. [Accessed 01/06/2024].

RIVM. Measurement station along N201. personal communication, 7 2023a. Acquired on 18-01-2024.

RIVM. Measurement station NL10641. personal communication, 8 2023b. Acquired on 24-04-2024.

RIVM. Distant-dependent measurement near Haarrijn service station. personal communication, 5 2024. Acquired on 03-05-2024.

K. Sabaliauskas, C.-H. Jeong, X. Yao, Y.-S. Jun, P. Jadidian, and G. J. Evans. Five-year roadside measurements of ultrafine particles in a major canadian city. *Atmospheric Environment*, 49:245–256, 2012. ISSN 1352-2310. doi: https://doi.org/10.1016/j.atmosenv.2011.11.052. URL https://www.sciencedirect.com/science/article/pii/S1352231011012398.

D. E. Schraufnagel. The health effects of ultrafine particles. *Experimental amp; Molecular Medicine*, 52(3):311–317, Mar. 2020. ISSN 2092-6413. doi: 10.1038/s12276-020-0403-3. URL http://dx.doi.org/10.1038/s12276-020-0403-3.

C. Seigneur. *Air Pollution: Concepts, Theory, and Applications*. Cambridge University Press, June 2019. ISBN 9781108481632. doi: 10.1017/9781108674614. URL http://dx.doi.org/10.1017/9781108674614.

W. Smeets. Geraamde ontwikkelingen in nationale emissies van luchtverontreinigende stoffen 2023. Technical report, Planbureau voor de Leefomgeving, 2023.

P. Vineis and K. Husgafvel-Pursiainen. Air pollution and cancer: biomarker studies in human populations †. *Carcinogenesis*, 26(11):1846–1855, 08 2005. ISSN 0143-3334. doi: 10.1093/carcin/bgi216. URL https://doi.org/10.1093/carcin/bgi216.

Y. Wang, P. K. Hopke, D. C. Chalupa, and M. J. Utell. Long-term study of urban ultrafine particles and other pollutants. *Atmospheric Environment*, 45(40):7672–7680, 2011. ISSN 1352-2310. doi: https://doi.org/10.1016/j.atmosenv.2010.08.022. URL https://www.sciencedirect.com/science/article/pii/S1352231010006965. Air Pollution and Health: Bridging the Gap from Sources-to-Health Outcomes.

WHO. *World Health Statistics 2016 [OP]: Monitoring Health for the Sustainable Development Goals (SDGs)*. World Health Organization, 2016.

N. Yamamoto. Chapter 8 - bioaerosols in built and natural environments. In N. Yamamoto, editor, *Fundamentals of Bioaerosols Science*, pages 399–467. Elsevier, 2023. ISBN 978-0-12-824411-1. doi: https://doi.org/10.1016/B978-0-12-824411-1.00005-3. URL https://www.sciencedirect.com/science/article/pii/B9780128244111000053.

Y. Zhu, W. C. Hinds, S. Kim, S. Shen, and C. Sioutas. Study of ultrafine particles near a major highway with heavy-duty diesel traffic. *Atmospheric Environment*, 36(27):4323–4335, 2002. ISSN 1352-2310. doi: https://doi.org/10.1016/S1352-2310(02)00354-0. URL https://www.sciencedirect.com/science/article/pii/S1352231002003540.

A Appendix

The full GitHub repository this project is stored in can be found here: `https://github.com/Renseck/UFPy`. This contains a Python "wrapper" that drives the real HAM/SALSA2.0 model, and contains various functions for analysis and plotting purposes. Note that the model itself, that is required for this wrapper to function, is not freely shareable due to licensing limitations.

A.1 Resampling bins

The method described in Section 3.2 is a simple linear interpolation, assuming a linear distribution between boundaries. However, there is also a possibility of a more exhaustive method, which seeks out to preserve particle counts from the outset.

$$\alpha = \frac{x_2 - y_1}{y_2 - y_1}. \tag{3}$$

Here, x_1 and x_2 are lower and upper boundaries respectively in the SALSA2.0 system, and y_1 and y_2 are lower and upper boundaries for the SMPS system. To make sure particle counts are conserved, we integrate both the original distribution (in SMPS bins) and the resampled distribution (in SALSA2.0 bins), and divide by the ratio of the two.

This can be proved with a short calculation, where we use the bin boundaries defined by Figure 33. It holds that

$$\alpha_{tot} = \frac{x_2 - y_1}{y_2 - y_1} + \frac{y_2 - x_2}{y_2 - y_1} = \frac{y_2 - y_1}{y_2 - y - 1} = 1, \tag{4}$$

meaning that the full weight is unitary, and particle number is conserved.

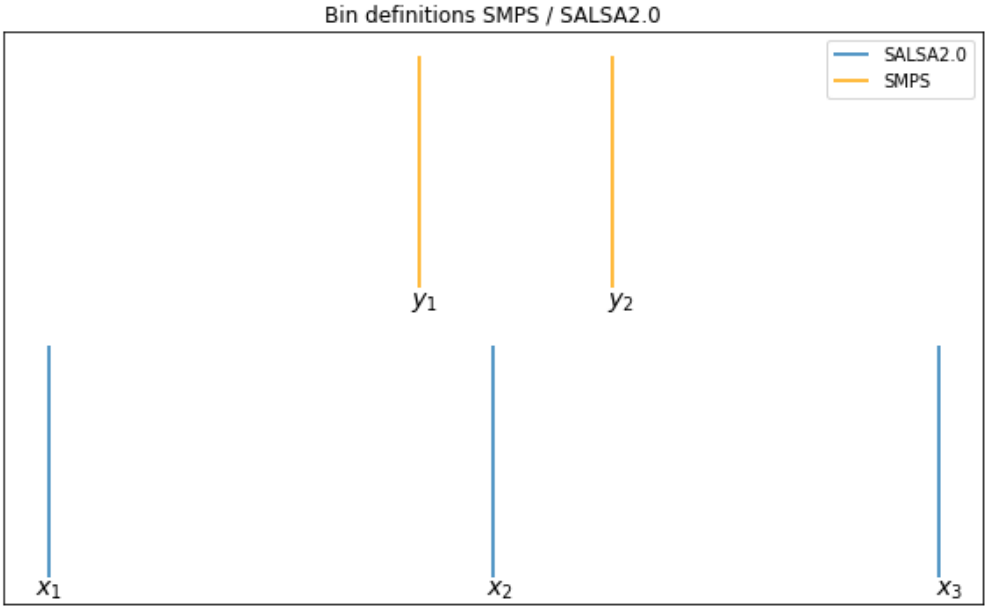

Figure 33: Schematic definitions of SMPS bins and SALSA2.0 bins.

A.2 Dispersion approximation

This calculation is based on private communications with Dr. Sjoerd van Ratingen, RIVM. The dispersion rate d is approximated based on a balancing of sources and sinks for a hypothetical box placed over a road. The source term is specified as a total number of particles added per second, and the sink is given by the dispersion rate; d particles leave the box every second.

Suppose the emissions take place in a box with a height of 3 m, width of 1 m (parallel to the road), and length of $L = 50\,\mathrm{m}$ (perpendicular to the road), giving it a total volume of $V_{box} = 150\,\mathrm{m}^3$. Based on effective emission factor of $3.34\,\mathrm{g\,km^{-1}}$ and a total of 120000 vehicles per 24 h, we estimate that the total emissions inside this box are $E = 4.0 \cdot 10^{11}$ particles s^{-1}. The box is ventilated with a wind speed of $v = 1\,\mathrm{m\,s^{-1}}$. Note that variations of this value will only adapt the equilibrium concentration. This wind blows into the "short", perpendicular side of this hypothetical box, meaning it displaces $Q = vA_\perp = 3\,\mathrm{m^3\,s^{-1}}$ of air. With a total volume of $150\,\mathrm{m}^3$, this immediately allows us to calculate the dispersion rate d, as

$$d = \frac{Q}{V_{box}} = \frac{vA_\perp}{LA_\perp} = \frac{v}{L} = 0.02 \tag{5}$$

This means that, for any concentration of particles, 2% of the particles will be leaving the box. Note that this is a little higher than the values we've used in the various simulations reported in Section 4, but this is only an approximation. We can solve a differential equation to precisely calculate the number of particles present in the box when equilibrium is reached. The starting differential equation for the rate of change of particles in the box is given by

$$\frac{dn}{dt} = -d \cdot n + E, \tag{6}$$

which has solution

$$n(t) = A \cdot \exp(-dt) + \frac{E}{d}. \tag{7}$$

The constant A can be expressed in terms of the initial particle concentration n_0, by $A = n_0 - \frac{E}{d}$, making the total solution

$$n(t) = (n_0 - \frac{E}{d}) \cdot \exp(-dt) + \frac{E}{d}. \tag{8}$$

Taking the limit of t to infinity, the solution reduces to the very simple form of

$$\lim_{t\to\infty} n(t) = \tag{9}$$

$$\lim_{t\to\infty} (n_0 - \frac{E}{d}) \cdot \exp(-dt) + \frac{E}{d} = \frac{E}{d}. \tag{10}$$

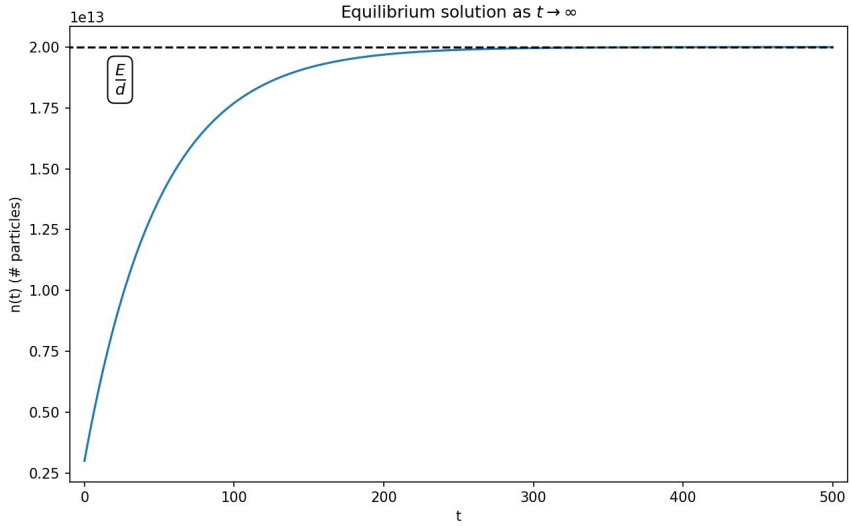

Figure 34: Plot of number of particles as function of time under constant emissions $E = 4.0 \cdot 10^{11}$ particles s^{-1} and dispersion $d = 0.02$. The blue line is the solution of the differential equation Equation 8, and the black dashed line is the limit value $\frac{E}{d}$.

In the case of the numbers used in the description of this box, this means that in equilibrium, there are $N = 2 \cdot 10^{13}$ particles in the entire box. Assuming these are homogeneously distributed (which is unlikely), this is equal to a particle number concentration of $133 \cdot 10^3$ particles cm^{-3}. This is considerably higher than what's measured along even busy highways.

A.3 MMR array

The exact structure of the MMR array responsible for tracking all particle numbers and compositions had to be elucidated before we could begin to implement a constant source, and the dispersion of particles throughout the system. A comprehensive note of this structure is given here, as considerable time was spent in decoding it. Furthermore, we present additional information on the exact implementation of the dispersion mechanismm.

The MMR array in question has length 108 for each horizontal and vertical grid cell, which is much more than the 17 size bins used by SALSA2.0, and notably not an integer multiple of 17 either. Below is a table that outlines the exact structure of the array. The index given in the first column starts counting at 1, as this is the convention used by Fortran90, the language the model is implemented in. All units are that of mass-mixing ratio.

MMR array details	
Index (inclusive)	**Contains**
1	Empty
2 - 3	SO_2 and SO_4 concentrations
4 - 6	Sulfate mass (bins 1a1 - 1a3)
7 - 9	Organic carbon (bins 1a1 - 1a3)
10 - 16	Sulfate volume (bins 2a1 - 2a7)
17 - 23	Organic carbon (bins 2a1 - 2a7)
24 - 30	Black carbon (bins 2a1 - 2a7)
31 - 37	Sea salt (bins 2a1 - 2a7)
38 - 44	Mineral dust (bins 2a1 - 2a7)
45 - 51	Sulfate volume (bins 2b1 - 2b7)
52 - 58	Organic carbon (bins 2b1 - 2b7)
59 - 65	Black carbon (bins 2b1 - 2b7)
66 - 72	Mineral dust (bins 2b1 - 2b7)
73 - 89	Particle counts (1a1 - 2b7)
90 - 106	Water content (1a1 - 2b7)
107 - 108	Empty

Table 2: Details of the MMR array responsible for tracking all particle numbers and compositions.

The indices 4 - 72 essentially function as the "composition" of the aerosol particles. The various compound classes have some overlap for each size bin, corresponding to the classes shown in Figure 4. At model initialisation, these are calculated according to certain weights, which preserve unity. For example, bins 1a1 - 1a3 have their mass divided into 20% sulfate and 80% organic carbon.

The exact implementation of the dispersion schematically represented by the blue arrows in Figure 6 relies on this structure, as not everything needs to be transported. We could not simply transport d% of the MMR array from grid cell 1 to grid cell 2, as that would also transport the gas background seen in indices 2 and 3, which we wanted to be constant throughout the system. An important realisation preceded the current implementation, namely that a doubling of particles also resulted in a doubling of all constituent compound classes as well; a linear relationship.

Every time step, a number of particles is added to the first grid cell of the model, by simple addition in indices 73 - 89. We calculate the percentage increase of this addition; say there are 1000 particles in bin 1a1 (index 73) and we add 100, that is a 10% increase. We then increase the corresponding "composition" indices as well, by the same percentage amount. This ensures that the composition of the particles remains the same, and is allowed to evolve further according to model mechanisms.